Instantaneous planar measurements of nitric oxide concentration in a turbulent n-heptane spray flame

Irfan Mulla, Gilles Godard, Bruno Renou

Instantaneous planar measurements of nitric oxide concentration in a turbulent *n*-heptane spray flame

Irfan.A. Mulla[a,b,*], Gilles Godard[a], Bruno Renou[a,*]

[a] *Normandie Univ., UNIROUEN, INSA Rouen, CNRS, CORIA, 76000 Rouen, France*
[b] *Department of Mechanical Engineering, Imperial College London, London SW7 2AZ, UK*

Abstract

Instantaneous and mean nitric oxide (NO) concentrations are measured in a turbulent, lifted, *n*-heptane jet spray flame at an atmospheric pressure using planar laser-induced fluorescence (PLIF). The flame-front is simultaneously located using OH-PLIF. The NO excitation line with the least temperature-quenching dependence is selected, and the associated NO-LIF dependence is corrected. LIF optimization and data reduction are based on previous work [Mulla et al. Combust. Flame 203 (2019) 217–229] where the NO-LIF signal was simulated at the spray flame condition (temperature and gas composition from LES) using a spectroscopic model. In the present work, to reduce interferences from polycyclic aromatic hydrocarbons (PAH) and soot, the detection bandwidth is progressively reduced from broadband (F6), intermediate (F3), to narrowband (F1). F6 results in a significant interference, while F1 contains the least interference. Instantaneous NO mole fraction (χ_{NO}) is deduced from F1 dataset using a novel instant-wise mapped interference subtraction approach (F1-Inst). The conditional mean NO concentrations derived from F6, F3, F1, and F1-Inst are in agreement (within uncertainty limits); however, F1-Inst appears to be the most reliable. Instantaneous flame-structure (OH) and NO concentration fields are analyzed. The spray flame structure consists of the inner (B1) and outer (B2) flame branches. Local extinctions are observed along B1. Small-scale

*Corresponding authors:
Email addresses: i.mulla@imperial.ac.uk (Irfan.A. Mulla), bruno.renou@coria.fr (Bruno Renou)

(< 1 mm) extinctions do not alter the NO concentration, whereas large-scale extinctions result in a sharp ($50 - 100\%$) χ_{NO} drop, possibly due to a reduced temperature. Instantaneous χ_{NO} along B2 shows a sharp growth until 55 mm height above burner (HAB), beyond which the growth saturates. The deceleration of NO growth and χ_{NO} reduction near the sooting region is most likely due to the soot-radiation induced temperature drop. Mean χ_{NO} along B1 measures $\sim$25 ppm with a small axial variation ($20 - 30$ ppm). Expected lower temperature and nearly constant χ_{NO} with residence time suggest the nitrous oxide and prompt NO formations routes. Mean χ_{NO} in the outer diffusion branch (B2) increases from 35 ppm at the flame-base to 75 ppm at 60 mm HAB. The NO growth and potentially high temperature in B2 indicate the thermal route of NO formation.

Keywords: Laser-induced fluorescence, Spray combustion, n-heptane, NO_x, Nitric oxide, Instantaneous NO concentration

1. Introduction

Spray flames exhibit a complex interaction between droplets, turbulence, and combustion. A large spatial variation of droplet size, flow velocity, and fuel concentration exists in spray flames [1]. This leads to the formation of a hybrid structure containing premixed, partially premixed, and diffusion flame branches [2]. The droplet-flame interaction also leads to local extinctions and heat release rate perturbations. These complex phenomena affect the formation of nitric oxide (NO) which is highly sensitive to the mode of combustion, residence time, and temperature. Therefore, to accurately predict the NO concentration, it is necessary to develop and validate thermochemical (and turbulence) models against an experimental database. Thus, physical insights and measurements derived from well-defined target flames are of great interest to the modeling community.

The *Turbulent Combustion of Sprays* (TCS) network [3] has been facilitating collaborations between experimental and computational communities. Since

its inception (in 2009), TCS has evolved from identifying target flames to establishing comprehensive databases in select flames. The target flames include a Sydney piloted dilute spray burner [4] and a Cambridge swirl spray burner [5]. The contribution by CORIA Rouen Spray Burner (CRSB) group has also been recognized. The CRSB database [1–3, 6, 7] includes spray shadowgraphy, droplet size and temperature, flow and droplet velocities, flame-front, ignition probability map, and mean NO concentration. So far, the TCS databases has primarily provided spray characterization, flow-field, and flame-structure information. There is a need to strengthen the database by measuring species concentrations, especially the pollutants such as NO and soot. The species measurements will contribute towards the validation of chemical kinetics mechanisms used in a large eddy simulation (LES).

In experiments, laser-induced fluorescence (LIF) is the most widely used technique to deduce NO concentration. However, the quantification of the fluorescence signal is very challenging due to a number of issues. 1) In addition to a probed species (NO) concentration, the fluorescence signal also depends on the mixtures composition (due to collisional quenching) and temperature (quenching cross-section, Boltzmann fraction, and density dependencies). 2) If the flame is fuel-rich, interference arises due to fluorescence from polycyclic aromatic hydrocarbons (PAH) and possibly from unburned hydrocarbons. In sooting flames, the laser-induced incandescence (LII) from NO excitation laser can exceed the NO-LIF signal, causing severe interference. 3) In spray flames, the Mie scattering from fuel droplets is several orders larger than the weaker NO-LIF. 4) Additionally, the complex turbulent spray flame structure (local flame extinctions and isolated flame islands) leads to a weakly defined flame-front, which poses difficulty in the data processing. The present spray flame contains all the above issues, which makes the accurate NO concentration measurement very challenging, even on the mean basis.

Quantitative NO measurements in gas phase mixture have been reported at atmospheric [8, 9] and elevated pressures [10–12]. At high pressures, additional interferences arise from LIF of O_2 and CO_2 [10] due to absorption line broad-

ening with pressure. A few studies provide quantitative NO concentration in two-phase automotive spray flames in diesel [13] and gasoline direct injection (GDI) [14–16] engines. In addition to O_2, CO_2, and H_2O interferences, the soot presence causes attenuation of the excitation laser and the NO fluorescence signal. The detailed steps of NO-LIF signal correction in a GDI engine are provided in Fissenewert et al. [15]. This elaborative description demonstrates the data reduction complexity in the evaluation of NO mole fraction. The interferences are much more severe in diesel engines [13], making the NO concentration deduction extremely challenging. Verbiezen et al. [13] incorporated attenuation correction in diesel engine through bidirectional LIF, absorption spectroscopy, and Raman scattering of N_2 [17]. Ottenwälder et al. [18] reported NO measurement in a high pressure n-heptane spray flame. The high injection and chamber pressures resulted in better mixing. Thus, the investigated spray flame [18] was largely non-sooting; consequently, PAH and LII interferences were not significant.

NO measurements in aeronautical sprays at elevated pressure were reported using LIF [19] and Laser-saturated fluorescence (LSF) [20] techniques. The LSF technique is considered to be insensitive to the gas composition, and therefore used by a few researchers [9, 21]. Nevertheless, the gas temperature must be known to deduce the NO concentration from the fluorescence signal. Another difficulty is that the larger fluence requirement restricts the LSF application to a point or line measurements. Additionally, LSF is applicable to only non-sooting flames, since a high fluence can lead to a significant LII interference.

Most of the past NO measurements in automotive and aeronautical sprays were performed at elevated pressures to simulate practical engines. The NO concentration data in an atmospheric pressure spray flame is quite rare. Our recent work [7] provides mean NO concentration in an atmospheric n-heptane spray flame. The lower signal levels (due to low laser fluence) and LIF interference from PAH and unburned hydrocarbons (due to broadband $230-320\ nm$ detection) could not yield instantaneous NO concentration. Therefore, the present work utilizes higher laser fluence and narrower detections. The proposed narrowband detection strategies mitigate the PAH interference, leading to better

signal quality of mean NO concentration. Additionally, a novel interference correction approach is proposed to deduce instantaneous planar NO concentrations. Instantaneous NO concentration fields are used to study the effect of local extinctions on NO and to discuss the spatial patterns between NO, PAH, and soot (due to LII interference). Thus, the present work contributes *i*) to the enhancement and validation of the previously reported mean NO concentration, *ii*) to the instantaneous NO concentration measurement and the elucidation of local extinctions effects on NO, and *iii*) to the identification of the soot and soot-precursor formation zones.

2. Experimental methods

2.1. Burner and Flame condition

A turbulent, lifted, n-heptane spray flame was stabilized on the CRSB facility at atmospheric pressure. The burner geometry was presented in the prior work [1]. The burner consists of a simplex injector (Danfoss, 1.35 kg/h, 80^o hollow cone) which was used to atomize the liquid-phase n-heptane. The co-flow of air was supplied around the injector through the annular opening of 10 and 20 mm diameters. The air flow rate of 6 g/s was maintained using a thermal mass flow controller, whereas the fuel flow rate of 0.28 g/s was regulated using a Coriolis flow controller. The air/fuel ratio corresponds to a global equivalence ratio of 0.71. This flame condition has been selected as a target case in prior works [1, 6, 7] following the flame stability tests.

Figure 1 shows the flame photograph along with the schematic illustrating the presence of expected species. The traversing laser beam in the photograph shows the Mie scattering from fuel droplets. The central core (non-reacting) region contains a large number of droplets, while fewer droplets are noted in the reacting regions. The flame stabilizes $\sim$25 mm above the burner. A double flame structure typically associated with the jet spray flame is observed. The blue flame-base suggests partial premixing, while the downstream region shows yellow luminosity from soot radiation suggesting non-premixed combus-

tion. Therefore, the soot-precursor (PAH) presence is anticipated upstream of the sooting region. Two view fields (VFs), H1 (r = 6–37 mm, z = 20–51 mm) and H2 (r = 9–40 mm, z = 45–76 mm), marked in Fig. 1 were used for NO imaging. The burner was translated using a 3-axis motorized stage. The schematic in Fig. 1 shows the OH-PLIF signal along with the expected zones of PAH, NO, and soot. This schematic is derived from the flame photograph and findings of the present work (Sec. 3.3). The H1 region appears soot-free, while the soot presence is noted in the downstream H2 region. The inner and outer flame branches are denoted ([2]) by B1 and B2, respectively, whereas Zone-C denotes the enclosed region.

2.2. Laser diagnostics

A total of 1500 OH/NO PLIF image pairs were acquired simultaneously at 3.3 Hz rate in the spray flame. The OH-PLIF was used to detect the flame-front (Appendix B.1), while the NO-PLIF was employed to evaluate the NO mole fraction. To subtract interferences, NO transition-detuned (while OH-tuned) PLIF signal (1500 images) was also acquired. Both the H1 and H2 fields measured 31 $mm \times 31$ mm, with a magnification of 33 $pixels/mm$. The laser diagnostics set-up was similar to our prior work [7] with a few improvements. Figure 2 depicts the laser diagnostics layout. A higher laser fluence was used for NO-PLIF in the present work. The OH and NO laser beams passed through the different set of light-sheet forming optics, providing independent control. Both the OH and NO light-sheets measured ~0.15 mm in thickness. The sheets were spatially overlapped in the measurement region. The laser energy can reduce as it traverses through the spray flame due to extinction or absorption by PAH, droplets, and soot. To minimize this effect, a portion of the flame towards the laser-incident side was imaged. During the simultaneous OH/NO acquisitions in the spray flame, an additional emICCD camera (PI-MAX®4: 1024 EMB, Princeton Instruments) simultaneously imaged NO-PLIF from a NO-seeded McKenna flame. The NO laser-sheet propagated over a McKenna flame towards the spray burner. The NO data from the reference flame provides

information on shot-to-shot energy fluctuation, wavelength/energy drift, and the spatial stability of the NO light-sheet profile.

The OH-PLIF system was identical to [7], where a detailed description is available. The $Q_1(6)$ line of A–$X(1,0)$ transition located near 283 nm was used to excite the OH radical. The LIF signal was imaged using a set of filters which transmits 315 nm with 15 nm bandwidth. The narrowband filter mitigated Mie scattering from fuel droplets and PAH-LIF interference. The camera was gated to 100 ns with respect to the laser pulse.

NO was excited using the $Q_1(29.5)$ line of A–$X(0,0)$ band (detailed subsequently). The NO-LIF signal was collected in different spectral ranges, namely F6, F3, and F1, resulting in three complementary datasets. The transmission curve of each detection filter is overlaid on the NO fluorescence spectrum in Fig. 3. The broadband (F6) NO-LIF measurements were performed with a different laser than the F3 and F1 detections. The mean fluence of NO laser-sheet for F3 and F1 datasets was 0.05 J/cm^2, while the fluence in the previous F6 dataset [7], was 0.02 J/cm^2. Linearity of the NO-LIF signal intensity at the present fluence (0.05 J/cm^2) was confirmed. The fluence in our previous work was limited by the available laser. The higher fluence in the present work enhanced the LIF signal quality compared to the prior measurement [7], which could not yield instantaneous NO concentrations due to low signal quality. However, the higher fluence results in LII interference which starts around 0.05–0.10 J/cm^2 [22]. In the present work, LII interference is noted in $z > 60$ mm region. Thus, in sooting flames, the laser fluence is a trade-off between the NO-LIF signal intensity and LII interference.

The NO-PLIF system for F3 and F1 measurements consisted of a frequency-doubled Nd:YAG laser (Quanta-Ray Pro-350-10, Spectra-Physics) which pumped a dye laser (PrecisionScan-LG-24-EG, Sirah) running with the mixture of Rhodamine 610 and Rhodamine 640 dyes. The Nd:YAG laser was injection seeded to obtain a narrow linewidth (0.005 cm^{-1} @ 355 nm). The dye laser fundamental output (615 nm) was mixed with 355 nm from the Nd:YAG laser, ultimately generating 225.12 nm (specified in a vacuum). The portion of the light-sheet uni-

form within 55% of peak intensity was used for the PLIF measurements. Before the spray flame measurements, the excitation wavelength was verified through the excitation/emission spectrum scan in a NO-seeded McKenna flame. The experimental spectrum was compared with the simulated spectrum obtained using LIFSim [24]. The excitation wavelength of 225.12 nm with 0.1 cm^{-1} laser linewidth was used to excite the $Q_1(29.5)$ transition of A–$X(0,0)$ band. The spectral bandwidth of the laser results in the excitation of multiple transitions, namely $Q_1(29.5)$, $R_2(25.5)$, $P_{21}(29.5)$, $Q_2(31.5)$, and $R_{12}(31.5)$. We refer to these combined transitions as $Q_1(29.5)$ for brevity based on the intensity relevance. The combined temperature-quenching LIF dependence of the $Q_1(29.5)$ excitation in the present spray flame was found to be the least out of other candidate transitions [7]. The NO-LIF optimization was based on the simulations of the LIF temperature-quenching dependence for various excitation wavelengths (transitions) at the spray flame condition. For LIF simulations, the CORIA LIF model [7, 23] was used. The temperature and gas composition needed for the LIF simulation were obtained from the spray flame LES data [2, 25]. The temperature within the investigated spray flame region typically ranges from 1200 to 2200 K. The excitation scheme should be optimized for a given flame condition and linewidth of the laser.

The NO fluorescence signal was imaged using an emICCD camera (PI-MAX®4: 1024 EMB, Princeton Instruments) equipped with UV lens (100mm f/2.8, Cerco). The camera was gated to 100 ns with respect to the laser pulse. In the prior work [7] broadband detection (F6) was used due to low signal intensity owing to a lower fluence (0.02 J/cm^2). The fluorescence detection between 230–320 nm allowed the imaging of six NO fluorescence bands, namely A–$X(0,1)$ to (0,6) as shown in Fig. 3. This detection is denoted by F6 (Filter transmitting 6 bands). Ideally, a narrowband filter isolating A–$X(0,1)$ band near 235 nm is preferred to reduce interferences. This approach has been implemented in non-sooting gas-phase [26, 27] and high-pressure spray [28] flames. However, in the present atmospheric spray flame, large droplets lead to significant Mie scattering noise. The blockage of the order of $< 1e{-}15$ @ 225 nm is needed to

eliminate the Mie scattering at the present fluence entirely. The filter should also maintain a sufficient transmission ($> 20\%$) at 235 nm with a very narrow bandwidth (ideally, < 2 nm as used in [28]). A filter with such demanding specifications was not available. Instead, we used two relatively narrower detection windows to reduce interferences. Figure 3 shows the transmission curves for all three detection schemes, namely broadband (F6), intermediate (F3), and narrowband (F1). The transmission values at NO-LIF bands are provided in Table A.3 (in the appendix) for each detection. The F3 detection collects signal from A–$X(0,1)$ to (0,3) bands using a stack of following six filters: two 224 nm long-pass edge filters (#LP02-224R-25, Semrock), 265 nm, 300 nm and 350 nm short-pass filters (#ZUS0265, #ZUS0300, #ZUS0350, Asahi Spectra), and a UG5 Schott filter. The F1 detection primarily collects fluorescence from A–$X(0,2)$ band using the following stack of filters: two 224 nm long-pass edge filters (#LP02-224R-25, Semrock), a 254 nm mercury line filter (#Hg01-254-50, Semrock), 300 nm and 350 nm short-pass filters (#ZUS0300, #ZUS0350, Asahi Spectra), and a UG5 Schott filter. To compensate for lower global transmission with F3 and F1, the higher fluence of 0.05 J/cm^2 was used. Measurements at higher fluence with F6 detection were not performed since the LII and PAH interferences would be significant. Instead, the earlier F6 data [7] with low fluence is used for comparison with F3 and F1.

The NO-LIF signal was calibrated against the NO-seeded flames in a McKenna burner, as detailed in Appendix C. Excellent linearity is observed between the NO concentration and LIF signal.

3. Results and discussion

3.1. Mean tuned and detuned signals in spray flame

The detuned signal was also acquired in the spray flame to assess interferences in NO-LIF. Figure 4 shows ensemble-averaged (unconditionally) tuned and detuned LIF signals for each of the detections. The previously reported F6 results [7] are also presented for comparison with F3 and F1. The flame-front

location is indicated by the mean progress variable ($\bar{c}$) contours, which are deduced from simultaneously acquired OH-PLIF images. The image processing method to deduce the flame-front and mean progress variable is detailed in our prior work [7] and also concisely provided in Appendix B.1. The OH-PLIF image is binarized using a certain (∼0.3 times of the peak) threshold. Occasionally, the flame-front is not continuous due to local extinctions [1] of the inner reaction zone (B1 branch). The broken OH segments are connected to the nearest neighbor. The connected reaction zones are marked by locating the centerline of the OH-layer. A progress variable map is deduced by defining $c = 0$ in the fresh gas and $c = 1$ in the burnt gas (Zone-C). Each OH-PLIF image provides an instantaneous c map, which is averaged over 1500 realizations to deduce the $\bar{c}$ map.

The comparison of the detuned and tuned signals provides interference estimates both in intensity and space. The extent of spatial containment of the detuned signal within the flame-fronts is verified using the $\bar{c}$ contours. The detuned signal is maximum in a burnt gas ($\bar{c} = 1$) and decreases towards the fresh gas (lower $\bar{c}$). With F6 detection, the detuned signal exists until $\bar{c} = 0.3$ contour, although low in intensity. Even outside $\bar{c} = 0.3$ region, a non-negligible detuned signal is present, which is not the case with F3 and F1 detections.

In non-sooting regions ($z < 60\ mm$), observed interference is likely attributed to broadband fluorescence from smaller PAH. There could be other interfering species, such as partially oxidized hydrocarbons, but its contribution may not be dominant due to UV detection ($< 320\ nm$). Condensed nanoparticle soot-precursors do not produce fluorescence or LII when excited at UV wavelengths [29]. Interferences from O_2, CO_2, and H_2O are negligible ($< 2\%$ at 200 *ppm* of NO) at atmospheric pressure as verified in fuel-lean McKenna flames (detailed in Appendix C.2). Therefore, PAH is probably the dominant contributor to the observed interference. Thus, in non-sooting regions, the detuned signal is hereinafter referred to as PAH-LIF.

The signal-to-noise ratio (SNR) of NO-PLIF is evaluated in a PAH-free McKenna calibration flame (at 100 *ppm* NO seeding). The ratio of the mean

(μ) to the standard deviation (σ) of the signal in a uniform NO region is used. The SNR of an instantaneous image measured 2.9 with F1 detection, while F3 provides a slightly better SNR of 3.6. These values are comparable to broadband F6 detection, where SNR was 3 (with 0.02 J/cm^2 fluence). In the spray flame, due to the absence of a uniform NO region, we evaluate the signal-to-background (SBR) ratio. The SBR is estimated by comparing the LIF intensity in a peak signal region ($r = 30$–$32\ mm$, $z = 46$–$49\ mm$ in H1 VF) with that of an area where NO is absent ($r = 33$–$36\ mm$, $z = 21$–$24\ mm$). The SBR in an instantaneous NO-PLIF image is 12 with F1, and 21 with F3. The enhanced signal quality with F3 and F1 is a result of the narrowband detection and the increased laser fluence relative to F6 where instantaneous SBR was only 3.5.

Although the signal intensity is lower with F1, the PAH interference is the least. To compare quantitatively, the detuned to tuned signal ratios are listed in Table 1 for various detections. The ratios are provided at $z = 42\ mm$ for different mean flame locations ($\bar{c} = 1,\ 0.9,\ 0.3$). The region of $\bar{c} = 1$ is wide, and thus the ratio is evaluated at a fixed peak PAH location of $r = 21\ mm$. Whereas, the radial locations for $\bar{c} = 0.9$ and 0.3 are 26–27 mm and $\sim$30 mm, respectively, across different detections (F6, F3, and F1).

As expected, the PAH-LIF interference is larger with the broadband F6 detection, both in intensity and in spatial distribution. Since the flame is sooting, the PAH presence is anticipated. The excitation and detection wavelengths of F6 suggests that the interference arises primarily from smaller PAH (1-3 ring), as indicated by Bejaoui et al. [30]. The interference reduces with an increase in r towards the fresh gas (lower $\bar{c}$). This is a result of the consumption of smaller PAH towards the formation of larger PAH [31] that do not produce fluorescence with UV excitation [30]. Larger PAH coagulate and subsequently go through thermochemical processes to form soot [32].

With the narrower (F3 and F1) detections, interference in the burnt gas region ($\bar{c} = 1$) decreases relative to F6, but not significantly. However, the interference reduces significantly towards the fresh gas (lower $\bar{c}$) with both the F3 and F1 strategies. As the detection range is narrowed towards deep-UV,

interference from relatively larger PAH [30] situated closer to flame-front is reduced. Thus, the lowest interference of 9% at $\bar{c} = 0.3$ is observed with F1. This implies that the NO measurements in the outer flame branch (B2) are nearly interference-free, at least in $z < 60\ mm$ region. Beyond $z = 60\ mm$, the detuned signal spreads outside of the $\bar{c} = 0.9$ contour for all the detections, namely F6, F3, and F1. Although the narrowband (F1) detection reduces the PAH interference, the increased fluence ($0.05\ J/cm^2$) leads to a strong LII interference from soot. The distinction between LII and PAH-LIF signatures is discussed subsequently in Sec. 3.3.6 using instantaneous detuned images. The soot interference is not significant with F6 due to lower fluence ($0.02\ J/cm^2$). Nevertheless, appreciable detuned signal (attributed to PAH-LIF and weak LII) exists between $\bar{c} = 0.9$ and $\bar{c} = 0.3$ in a region of $z > 60\ mm$. This comparison demonstrates that in a non-sooting, PAH-containing region, F1 strategy provides the least interference. To evaluate NO concentration, the detuned signal (interference) is subtracted from the tuned signal. Since the detuned signal in a region of $z > 60\ mm$ spreads outside of the mean flame-front, we retain the data only till $z = 60\ mm$. In a sooting environment, laser fluence cannot be increased beyond a certain threshold due to LII interference.

3.2. Conditional mean NO concentration

To obtain quantitative NO concentration, intricate data processing steps are followed in an identical manner as in [7]. For further clarity, processing flowcharts detailing each of the steps are provided in Appendix B. The main components of the data processing are: 1) Flame-front detection, 2) Detuned signal subtraction from NO transition-tuned signal, 3) NO-LIF signal calibration, and 4) LIF temperature-quenching correction.

The NO-LIF data bounded by the flame-fronts is considered for conditional averaging since NO concentration is negligible in the fresh gas. Thus, the first step is to detect the flame-front using OH-PLIF, as detailed in Appendix B.1. The raw image is corrected for background and light-sheet profile. The corrected OH-PLIF image is mapped (pixel-by-pixel) to the NO-PLIF image through

the second-degree polynomial transformation using a calibration target. The spatially transformed OH-PLIF image is used to deduce a progress variable similarly, as discussed in Sec. 3.1. The progress variable definition leads to $c = 0$ in fresh gas and $c = 1$ in burnt gas (Zone-C).

The NO-LIF signal (I_{NO}) only within the $c = 1$ region is considered for conditional averaging. The flowchart in Fig. B.20 provides detailed processing steps. The background signal (mainly attributed to the camera dark-noise) is subtracted from respective NO transition-tuned and -detuned images. The instantaneous tuned images are median filtered (3×3 $pixels$) to reduce the shot-noise. Both the tuned and detuned images are corrected for respective light-sheet profiles. Next, the mean detuned signal is subtracted from the NO transition-tuned signal. Subsequently, the LIF calibration and temperature-quenching correction are applied. Finally, the corrected instantaneous NO concentration fields are conditionally averaged. The condition is to consider the data only within the $c = 1$ region for a given instant. The additional condition is to consider only the locations with at least 200 conditional samples out of 1500 laser shots.

The calibration and LIF temperature-quenching correction involve the use of three different simulations, namely Cantera, the LIF model, and spray flame LES. Cantera and LES provide the gas composition (of LIF quenching species) and temperature, in McKenna calibration and spray flames, respectively. This information is fed into the LIF model to evaluate the temperature-quenching dependence. The data processing protocol is the same as of [7], steps of which are detailed in the appendix (Figs. B.19 and B.20) and also concisely described here.

The LIF signal, I_{NO} is converted to a relative mole fraction by using the McKenna calibration constants (derived from Appendix C.1) as, $\chi^R_{NO} = C_1 I_{NO} + C_2$. The relative concentration is converted to an absolute χ_{NO} by applying the LIF temperature-quenching correction. The LIF intensity per unit mole fraction of NO at the McKenna calibration flame condition (S_{f+}^{McK}) is obtained using the CORIA LIF model [7, 23]. The LIF model takes into account the

excitation wavelength, laser linewidth, and filter transmission. The gas composition and temperature needed to simulate S_{f+}^{McK} are obtained by simulating the burner-stabilized flame with Cantera [33].

The LIF intensity per unit mole fraction of NO at the spray flame condition (S_{f+}) is also obtained. To simulate the LIF signal, it is necessary to know the gas composition (major NO-LIF quenchers) and temperature a priori, which are obtained from the LES data [2, 25]. In the spray flame, the gas composition and temperature are spatially inhomogeneous, which leads to a variation of NO-LIF intensity even at a fixed NO concentration. As demonstrated in [7], the radial variation of S_{f+} is appreciable; however, the axial variation is not significant with the $Q_1(29.5)$ excitation. Therefore, only the mean radial variation of LIF dependence (S_{f+}^{m-c}) is accounted for. S_{f+}^{m-c} is obtained in the following manner. From the LES data, only the region bounded by inner and outer flame branches is considered, similar to the experimental data (NO-PLIF) processing. S_{f+} profiles at various axial stations are averaged (in flame-branch B1/B2 fixed coordinates) to obtain an axially-averaged radial correction curve S_{f+}^{m-i}, where superscripts m and i denote axial-mean and instant-number, respectively. Such, S_{f+}^{m-i} curves are evaluated at 15 LES instants (snapshots), which are used to deduce a conditionally averaged LIF dependence (S_{f+}^{m-c}). Recall, S_{f+}^{m-c} is a function of radial distance conditioned using inner and outer branch locations of the simulated spray flame. Next, the normalized LIF dependence is expressed as, $S_{f-N}^{m-c} = S_{f+}^{m-c}/S_{f+}^{McK}$. To correct the NO-LIF dependence, the S_{f-N}^{m-c} profile is radially mapped to the experimental (S_{f-N}^{E}) flame branch radial locations (deduced from OH-PLIF). In this manner, spatial differences between simulated and experimental flames are accounted for. Finally, the absolute NO mole fraction is obtained as, $\chi_{NO} = \chi_{NO}^{R}/S_{f-N}^{E}$. This approach has been validated and detailed in our recent work [7].

Figure 5 shows the conditionally averaged absolute NO mole fraction (χ_{NO}) obtained through the sophisticated data reduction. The total uncertainty of $\pm 30\%$ is estimated in mean χ_{NO}. The uncertainty originates from the following sources: 1) NO calibration, 2) Fluctuations associated with the flow/flame, laser,

and camera, 3) Extinction of NO excitation laser and NO fluorescence trapping, and 4) LIF temperature-quenching correction residual. A detailed discussion of uncertainty is available in [7]. The measurements yield mean NO (in *ppm*) at two heights, namely H1 and H2. The values in overlapping regions are averaged to obtain the composite mean field. For the spatial reference, contours of mean progress variable ($\bar{c}$ = 0.1, 0.5, and 0.9) are overlaid. The previously reported χ_{NO} with F6 is compared with the present F3 and F1 detections. The mean light-sheet profile during the spray flame campaign was simultaneously monitored as stated in Sec. 2.2. During F6 experiments light-sheet remained spatially stable during the whole (spray flame and calibration) campaign. But, in F3 and F1, different laser and light-sheet optics were used. The shot-to-shot laser pointing instability caused a minute spatial drift in the laser-sheet between the tuned, detuned, and calibration campaigns. This is accounted in the post-processing through the respective light-sheet profile correction on the mean basis. Yet, a minor residual remains along the outer branch in F3 case. This was not an issue for F1 since the narrowband filter readily minimizes the interference.

Overall, an excellent agreement of inferred NO concentration is observed between F6, F3, and F1 from Fig. 5. χ_{NO} along the inner branch (B1) appears to be nearly identical for all three detections. However, χ_{NO} with F6, around z = 50 mm along the outer branch (B2), measures a slightly lower than that with F3 and F1. Additionally, with F6, the NO concentration within $\bar{c} = 0.9$ in z = 35–50 mm zone, appears higher than that of F3 and F1. Although these differences are within the uncertainty ($\pm$30%), deviation in NO concentration with F6 is primarily attributed to the unconditional PAH subtraction. Recall, F6 uses lower laser fluence and broadband detection, resulting in relatively poor signal quality and more noise (due to interference and shot-noise). In principle, the detuned subtraction should account for the interference, but any fluctuations in the laser energy and camera dark-noise could lead to errors, especially with a weaker signal.

A region of low NO is observed around r = 16 mm, z = 30 mm with all

the detections. As discussed previously [7], low temperature resulted from local extinctions of the B1 branch is likely responsible for the low NO zone. In F3 and F1, an additional region of low NO at z = 40–60 mm, r = 16–20 mm, is observed. This is not clearly observed with F6 detection due to lower SBR. The low NO zone progressively becomes evident with narrowing of the spectral window (from F6 to F1). The interior region (Zone-C) possess a relatively lower temperature and does contain primarily the fuel vapor without oxygen [2], which could be the cause of low NO. This low NO region is in the vicinity of B1 branch, and thus, the local flame extinctions of B1 could also lower the NO concentrations. The definitive conclusions cannot be drawn from mean NO results alone. Nevertheless, the hypothesis is confirmed from instantaneous NO concentration fields, as demonstrated subsequently in Sec. 3.3.5. Further discussion on the NO formations in the B1 and B2 branches is continued in Sec. 3.3.8 along with the additional result from the F1-Inst dataset.

The observations/discussion in the present section and the Sec. 3.1 lead to the following preliminary conclusions from the diagnostics point of view. The use of high fluence is necessary to increase the NO-LIF signal intensity relative to the camera dark-noise and photon shot-noise. In non-sooting and aromatic-free regions, all three strategies F6, F3, and F1 can be employed with high laser fluence. However, in the PAH-containing regions, the use of the F1 strategy is recommended due to the least interference. F3 is a compromise between the NO-LIF signal and PAH interference. For practical (aromatics-containing) fuels, F3 or F1 detection can be employed instead of broadband F6 to mitigate the fluorescence interference from non-reacting fuel. In a sooting region, low fluence ($< 0.02\ J/cm^2$) and narrower detection (F1) with high collection efficiency are recommended to mitigate the LII interference. Out of the three detections, F1 provides the most reliable data since it contains the least PAH interference and high SBR (partly attributed to high fluence). Therefore, F1 dataset is exploited further to evaluate instantaneous NO concentrations.

3.3. Instantaneous NO concentration

The mean NO concentration provides insight into global behavior; however, in a fluctuating field, local information is lost in the averaging process. The spray flame structure is highly complex due to local extinctions [1], soot presence, and large variability of fuel concentration field due to evaporating fuel droplets. Only instantaneous measurements can conclusively reveal the impact of local extinctions and soot radiation on the NO concentration. Additionally, the spatial correlations between PAH, soot, and NO distribution can be derived from instantaneous images. Such correlations are not accessible from the mean image since the gradients are diffused due to fluctuations. To evaluate instantaneous NO concentration, the PAH interference poses a significant challenge. Although the F1 detection nearly eliminates PAH interference near the outer flame branch, it remains appreciable in the burnt gas region (see Fig. 4f). To circumvent this issue, we incorporate a novel instant-wise PAH conditional subtraction as detailed subsequently.

3.3.1. OH at H1

The experiments were performed at two different heights (lower H1, and upper H2) as explained in Sec. 2.1. Figure 6 shows a few OH-PLIF instants at H1 along with the OH-isocontour. Arbitrary camera coordinates are used with pixel units for convenience. These OH-PLIF images are simultaneously acquired during the detuned NO-LIF campaign. The flame-front is located by following the centerline of the OH layer as discussed earlier in Sec. 3.1. The detected flame-front is used to deduce a PAH conditional map. As demonstrated through the flame-index fields [2], the inner branch B1 is composed of two reaction zones namely lean premixed (B1-P) and adjacent non-premixed (B1-D). B1-P lies towards the fresh reactant side of B1, while B1-D is situated towards the product side (Zone-C) of B1. Such structure is unique to the spray flame. Combustion in the outer branch (B2) occurs largely in a diffusion mode. Local extinctions are observed along B1 due to high flow strain rate and heat loss to traversing fuel droplets [1]. In the outer branch B2, fuel droplets reduce OH-

LIF signal, but no local extinctions are noted. The B2 (pure diffusion) branch is more resilient to extinction due to low strain rate and high temperature [2] relative to the composite B1 (lean/diffusion) branch.

3.3.2. PAH mapping at H1

A PAH conditional map is deduced to enable the PAH-LIF interference subtraction from instantaneous NO-tuned (@225.12 nm) LIF signal. The procedure of mapping is illustrated with a flowchart in Appendix B.4, which primarily consists of following steps: 1) Flame-front detection, 2) Stretching detuned signal to a fixed radial range, 3) Signal discretization to a fixed radial spacing.

Instantaneous NO-detuned (@225.386 nm) samples containing PAH-LIF noise at H1 are shown in Figs. 7a to 7c along with the respective OH isocontours for the spatial reference. Since PAH is primarily contained within the flame branches, the signal outside of the OH-centerline is not retained. The flame-base and radial distances between B1 and B2 vary from instant-to-instant and also with height. To account for the spatial variation, the PAH signal at each z location is radially stretched in flame-fixed coordinates to a fixed radial range. At this stage, the stretching only alters the radial distribution and not the signal intensity. Next, the signal is discretized to a constant radial spacing to enable conditional averaging. A shape-preserving piece-wise cubic interpolation is used for the discretization, which introduces an uncertainty of $\pm 5\%$. Figures 7d to 7f show the instantaneous PAH maps relative to the flame-front. Note that the axial distance of $z_f = 1$ *pixel* in Figs. 7d to 7f corresponds to the flame-base. The radial locations of the inner and outer branches are marked by $r_f = 100$ *pixel* and $r_f = 900$ *pixel*. The radial stretch range (100–900 *pixel*) is arbitrarily selected. The distance between the flame-base and top edge of the field changes due to axial fluctuations of the flame-base. Therefore, in some of the PAH maps the data at higher heights is not available (white space).

For PAH mapping, inner (*r-in*) and outer (*r-out*) branch locations at each axial (z) distance are needed. Occasionally, at certain z, the flame-front has multiple values of *r-in* or *r-out* due to flame-wrinkling. These axial locations

are not considered to simplify the data reduction. This does not affect the conditional mean PAH mapping since a total of 1500 images are available for conditionally averaging. The mean PAH map is shown in Fig. 8 along with the labels to clarify the location of the flame-base, the inner and outer branches, and the axial distance above the flame-base. The PAH-LIF intensity in the mean map is lower than that of the instantaneous images by nearly a factor of two. This is attributed primarily to the random shot-noise in instantaneous images, which is mitigated in the averaging.

The PAH map is used to incorporate instant-wise PAH subtraction from NO transition-tuned LIF signal. The implicit assumption is that the PAH spatial distribution (relative to flame-fronts) and the intensity is identical across different instants. However, fluctuations in the signal can be observed from Figs. 7d to 7f. To evaluate the impact of this fluctuation on NO-LIF correction, PAH-LIF intensity in mapped instantaneous fields (e.g., Fig. 7d) is analyzed. Intensity in the vicinity of B2 branch is averaged in the region of $r_f = 350 - 450$ *pixel*, $z_f = 300 - 500$ *pixel*. The spatial averaging was performed to reduce the effect of shot-noise. Uncertainty due to shot-noise is considered subsequently. Variation of the area-averaged PAH intensity over 1500 shots is characterized through the standard deviation (σ) which measured 24% of the mean (μ). Similar analysis in Zone-C ($r_f = 350 - 450$ *pixel*, $z_f = 300 - 500$ *pixel*) leads to σ/μ of 13%. For a 95% confidence interval (CI), PAH-LIF uncertainty is $\pm 44\%$ near B2 and $\pm 26\%$ in Zone-C. Thus, the instant-wise PAH subtraction from the tuned signal (discussed next) can have a residual PAH. Nevertheless, with F1, the mean detuned signal is only 10% (recall Table 1) near the flame-front ($\bar{c} = 0.9$) and 44% in Zone-C. Consequently, the uncertainty in NO concentration due to PAH fluctuation is $\pm 4\%$ near B2 and $\pm 11\%$ in Zone-C.

3.3.3. Instant-wise PAH subtraction

The mean PAH map obtained in the previous section (Fig. 8) is used to implement the instant-wise PAH subtraction from the NO transition-tuned LIF signal. During the acquisition of the tuned signal, OH-PLIF images were also

acquired simultaneously to deduce the flame-front. The mean PAH map (Fig. 8) is spatially transformed to match the flame-front coordinates of a given instant using the following references. The flame-base provides the axial reference, while the radial references are obtained from inner and outer branches. At each z-locations of a given NO-tuned LIF image, the radial positions of inner (r-in) and outer (r-out) flame branches are recorded. The PAH profile at the considered z-location is extracted from the mean PAH map and radially scaled to match r-in and r-out of the given NO-tuned LIF instant. Subsequently, the mapped PAH signal is subtracted from the tuned signal.

Figure 9 shows the NO transition-tuned LIF signal containing PAH contribution, and the corresponding PAH-subtracted NO-LIF signal. The instant-wise PAH subtraction strategy indeed appears very promising, but as stated in the previous section the residual PAH-LIF contribution may be present. However, the primary issue arises from the shot-noise which is unavoidable even in a flame without any interferences. Therefore, the residual PAH-LIF is of secondary concern. There are recognizable spatial patterns in the PAH subtracted instantaneous NO image (Fig. 9b), which are discussed subsequently.

3.3.4. Uncertainty in instantaneous NO concentration

Uncertainty in mean NO concentration was estimated to be ±30% in [7]. Additional error sources relevant to instantaneous measurements are assessed as follows.

1. Uncertainty in PAH map due to the warping process is expected to be ±5%. The PAH map needs to be re-warped to enable the instant-wise PAH subtraction. Therefore, the combined uncertainty from warping is ±7%.
2. Since the mean PAH map is used for instant-wise subtraction, shot-to-shot fluctuations of PAH-LIF lead to uncertainty of ±11% in NO concentration, as detailed earlier in Sec. 3.3.2.
3. The photon shot-noise leads to a significant pixel-to-pixel variation of the signal, even with the uniform NO concentration. To estimate this uncertainty, SNR evaluated in McKenna flame (recall Sec. 3.1) can be used. SNR

of 2.9 with F1, translates to ±68% uncertainty (with a 95% CI). Note that the uncertainty due to shot-noise in instantaneous data can be minimized through spatial-averaging, rather than interpreting data at a single pixel. For instance, data averaged within a square region of 10 *pixel* size (0.3 *mm*) will reduce the uncertainty from ±68% to ±7%.

4. Fluctuations of gas composition and temperature can influence the mean-based LIF temperature-quenching correction. As shown in [7], instant-to-instant variation of axially-averaged radial LIF dependence (S_{f+}^{m-i}) is negligible. The variation of S_{f+}^{m-i} is within ±5% of the conditional mean (S_{f+}^{m-c}) in the spray flame. Moreover, the deviation of the axial LIF dependence (in instantaneous data) from S_{f+}^{m-c} is found to be primarily within ±10%. Therefore, S_{f+}^{m-c} is used to correct the LIF dependence of instantaneous measurements as well. Note that this source (±10%) has been accounted for in our earlier uncertainty estimate of ±30% [7].

Based on the uncertainty propagation, the combined uncertainty in instantaneous NO at an individual pixel is ±75%, while it reduces to ±33% when a square region of 10 *pixel* size (0.3 *mm*) is considered. Therefore, instantaneous NO data at a single pixel is treated to be semi-quantitative, while area-averaged values are quantitative.

3.3.5. Instantaneous NO concentration at H1

To obtain instantaneous NO concentrations, the PAH subtracted NO-LIF signal requires multiple corrections as illustrated in Appendix B.5. The following corrections are applied: 1) Light-sheet profile, 2) LIF temperature-quenching correction, 3) Shot-to-shot laser energy fluctuations (±11% with a 95% CI), and 4) NO calibration.

Instantaneous absolute NO mole fraction (in *ppm*) fields are shown in Fig. 10. The physical burner coordinates are used. The NO detectability limit appears to be ∼5 *ppm*, based on SBR described in Sec. 3.1. The OH isocontour (3500 counts) is overlaid in magenta color for the flame-front reference. The local extinction regions are highlighted by the ellipses in cyan. The local extinction

probability of ∼50% is derived by analyzing breaks (extinctions) in each of the 1500 OH-PLIF images. The isocontour of 3500 counts was used (∼0.3 times of the peak intensity) to determine local extinctions. The image processing algorithm is identical to [7]. The effect of extinctions on local NO concentration is investigated by analyzing 200 instantaneous images. A representative value of 25 *ppm* mean NO concentration along the B1 branch is used as a reference. Recall that the area-averaged instantaneous NO concentration is accurate within ± 33%. NO is considered to be appreciably influenced when χ_{NO} decreases below 50% from the base value of 25 *ppm*. Based on the extinction scales and NO response, the images are divided into different classes as indicated in the caption of Fig. 10. The probability of occurrence of each event-type is provided in terms of percentage of the total number (200) of analyzed images. The following four event classifications are considered.

1. NO concentration fields without any local flame extinctions are shown in Figs. 10a to 10c. The NO concentration is higher in the outer branch B2, whereas lower concentration is observed along the inner branch B1 and interior (Zone-C) of the flame.
2. Instances with small-scale local extinctions of the inner branch are shown in Figs. 10d to 10f. The scale of extinction is defined from the OH contour. Any breaks less than 1 *mm* are referred to as the small-scale extinctions. These extinction regions are highlighted by the ellipses. The NO concentration appears to be unaffected by these minor extinctions. Since the small-scale extinctions are about the flame thickness, the temperature may not decrease significantly, and thus sustaining NO at minor extinction locations. This type of extinction is observed quite frequently (35% probability).
3. Figures 10g to 10i show the instants with large-scale (> 1 *mm*) extinctions, where the NO concentration is negligible. These large-scale extinctions can lower the temperature significantly (even below prompt-NO formation limit), resulting in a sharp decrease in NO. We obtained quantitative estimates by analyzing such 20 images. The χ_{NO} values are averaged within a small region of interest (ROI) in the vicinity of large-scale extinctions. ROI size is adapted

to the scale of each extinction event. Typical ROI is 1 mm tall and 0.5 mm wide, which provide enough pixels for averaging to ensure the uncertainty within $\pm$ 33%. The results reveal that with large-scale extinction, χ_{NO} decreases from 25 ppm (mean base value) to $0-12$ ppm range (reduction of 50 to 100%). On an average, χ_{NO} decreases to 5 ppm (about 80% of reduction). The probability of such large-scale extinctions is low (10% probability).

4. At a few occasions (5% probability), higher NO concentration exists despite the large-scale local extinctions. These extinctions are marked by an ellipse with a dashed line in Figs. 10i to 10k. A few possible reasons for this behavior are - *a*) extinctions are imaged in a plane, whereas out-of-plane flame-front may not have been locally extinct, *b*) NO may get transported from other zones to the locally quenched regions, *c*) the rate of growth of extinction hole may exceed the timescales NO formation/response and that of thermal diffusion. This could be the likely reason for non-negligible NO concentration despite the local quenching. Although, it cannot be confirmed since the present low repetition rate (3.3 Hz) data do not provide the temporal evolution of local extinctions.

3.3.6. PAH and soot interferences at H2

Similar to H1, instantaneous detuned images at H2 are analyzed. Figures 11a to 11c show the OH-PLIF signal along with an isocontour in magenta. The outer branch shows a thick and diffused OH layer, whereas the inner branch appears wrinkled with a large variation of OH-layer thickness. At H2, the frequency of local extinctions of the inner branch is much lower (3% for z = 46–50 mm and 0% for $z > 50$ mm) than that of at H1 (50% probability). This is due to the reduced strain rate in the downstream region [1] and lower occurrence of droplet-traversing across the B1 branch at H2.

In the upper parts of H2 field, the flame is sooty as also evident from the yellow flame appearance in Fig. 1. The present laser fluence of 0.05 J/cm^2 can trigger the LII from mature soot particles. This can be observed from the NO-detuned signal shown in Figs. 11d to 11f. Unlike PAH, the soot structures are

highly localized due to high Schmidt number of soot particles, which leads to a low soot diffusivity [34]. The LII is much stronger and more intermittent than PAH-LIF. The contrasts in the signal intensity and spatial diffusivity provide an excellent way to distinguish PAH and LII contributions in NO-LIF.

A number of observations can be made from the NO-detuned images. The PAH-LIF intensity near the outer flame branch is diminished relative to H1. In the radially upstream region of soot, the imaged smaller PAH get converted to larger PAH which do not get excited in UV, and thus, the lower PAH-LIF intensity is observed. This is clearly visible in the mean PAH map (Fig. 12) around $z = 50\ mm$. The LII signal from soot is radially located between the PAH-zone and OH-layer (flame-front). The soot structure appears in a filament form, while PAH is spatially diffused. There is almost no signal between the soot-layer and outer flame branch. The radial sequence from the fuel injector is as follows: fuel, B1 reaction zone, PAH, soot, and B2 flame branch. Such radial order is analogous to a laminar counterflow diffusion flame [35]. The LII signal is high in intensity (relative to NO-LIF) despite the narrowband (F1) detection. Note that the PAH signal is well-aligned with the LII structure, even in the upstream regions where no LII is apparent. The absolute soot concentration was measured in a separate work [36]. The soot particles were heated with 1064 nm at 0.35 J/cm^2 fluence, and the LII signal was collected at 400 nm with 25 nm bandwidth. The soot-inception was found to occur around $z = 50\ mm$ height, well-upstream of the present observation (Fig. 11). The present low fluence (0.05 J/cm^2) and deep-UV (230–250 nm) detection may not image the upstream nascent soot.

The OH-LIF signal along B2 in Figs. 11a to 11c reduces sharply with height (in the soot presence), unlike that of H1 (Figs. 6a to 6c). The time-averaged peak soot volume fraction (f_v), standard deviation, and conditional mean (isolating soot intermittency) values from [36] are listed in Table 2. The statistics are evaluated at $z = 60$ and 76 mm, while the radial location ($r = 22$–$27\ mm$) corresponds to a peak value of the respective quantity. These f_v values are unlikely to result in a significant temperature drop. Based on [37], tempera-

ture reduction around 50 K is expected. Thus, the soot radiation alone cannot explain such a significant decrease in OH. The OH reduction is attributed primarily to soot oxidation reactions and only to a lesser extent to soot radiation losses, as demonstrated by Puri et al. [38]. Although there are other species, OH is the dominant soot oxidizer [38, 39], which explains the present OH reduction.

Next, the mean PAH-LII map is deduced at H2 (Fig. 12) identically to H1. The LII interference appears around $z = 60$ mm near the outer branch in Fig. 12. The soot interference is significant and localized compared to the PAH-LIF. Additionally, instantaneous LII structures in turbulent flames are highly intermittent. Consequently, the instant-wise LII noise subtraction will not be accurate, unlike the PAH subtraction. Nevertheless, the detuned subtraction until $z = 60$ mm (in the entire radial domain) and along the inner and outer flame-branches (where PAH and soot are negligible) over the entire height of VF is valid.

3.3.7. Instantaneous NO concentration at H2

Figures 13a to 13c show the NO transition-tuned instantaneous LIF images along with the OH isocontour. The images contain the LIF signal from NO, and interferences from PAH-LIF and LII. An appreciable signal is observed between the soot-layer and outer flame-front (OH), unlike that of the detuned signal (Figs. 11d to 11f). Thus, the tuned signal between soot and OH contains contribution primarily from NO. Therefore, at least in the outer branch B2, the PAH and LII interferences are negligible. Similarly, the PAH and LII interferences are low (see Fig. 12) along the inner branch B1.

The mean PAH-LII map (Fig. 12) is used to subtract the interference. Figures 13d to 13f show the mean detuned signal subtracted instantaneous NO-LIF images. The PAH-LIF noise is largely eliminated, however, a significant residual LII and correction artifact remain. Nevertheless, the NO concentration in Figs. 13d to 13f is valid along the entire outer branch (within the region bounded by OH-isocontour of B2), where PAH and soot are absent. The NO concentration is also valid along the entire B1 branch because of the negligible

PAH and soot presence. In the remaining portion of the radial domain (Zone-C), the NO concentration is valid only below $z = 60\ mm$ (low-sooting region).

The NO concentration along the inner branch B1 and in the vicinity is lower relative to B2. NO along the outer branch measures substantially higher, but nearly constant with height, suggesting a growth saturation unlike that of at lower height H1. The lower temperatures owing to soot radiation losses could lead to NO growth saturation. The growth saturation is also confirmed subsequently in a mean χ_{NO} (Fig. 17), where the discussion is continued.

3.3.8. Conditional mean NO based on instant-wise PAH subtraction

The instant-wise PAH subtracted instantaneous NO concentration images (e.g., Fig. 10 and 13) deduced from F1 dataset are conditionally averaged over 1500 realizations to provide a mean NO field. This data reduction strategy is denoted as F1-Inst. The mean NO concentration from F1-Inst is shown in Fig. 14. The composite image is obtained from H1 and H2 data. The data beyond 60 mm height is not retained due to higher LII noise.

The mean χ_{NO} from F1 (Fig. 5c) and F1-Inst are almost identical, as expected since the LII noise is not significant below $z = 60\ mm$. However, there are subtle differences between F1 and F1-Inst. As noted earlier, with F1 a very low χ_{NO} patch is observed around $z = 40$–$60\ mm$, $r = 16$–$20\ mm$ region, while with F1-Inst (Fig. 10) the χ_{NO} at this location is slightly higher ($\sim$20 ppm). As discussed earlier (Sec. 3.2) the low NO region is the consequence of local extinctions and oxygen scarcity.

To facilitate the comparison, axial and radial NO profiles are plotted for all the datasets namely, F6, F3, F1, and F1-Inst. The axial profiles are obtained by spatially averaging the data within $\bar{c} = 0.45$ to 0.55 region. The deduced profiles are shown in Fig. 15 along with the uncertainty ($\pm$30%). The radial profiles are plotted in Fig. 16 at $z = 38\ mm$ and $z = 55\ mm$. These profiles are obtained by averaging the data within $z \pm 0.5\ mm$ region. The profiles in both Figs. 15 and 16 are smoothed (using a Savitzky–Golay filter) for better visualization. The raw (unfiltered) profiles are provided in Appendix D.

Along the inner branch (B1), NO profiles from F1 and F1-Inst are in agreement, as noted from Fig. 15a. However, F3 and F6 detections show higher NO concentration which is attributed to the PAH interference and associated unconditional subtraction errors, as discussed in Sec. 3.2. Along the outer branch (B2), NO concentrations obtained from F3, F1, and F1-Inst are in close agreement, as evident from Figs. 15b and 16. The NO concentration in B2 (Fig. 15b) with F6 is consistently lower than that of other detections (F3/F1/F1-Inst). This is again attributed to the PAH subtraction errors. In the low PAH region (near $z = 55\ mm$), NO concentration from F6 converges to the rest of the datasets as observed from Fig. 15b. In all the plots (Figs. 15 and 16) for $z < 60\ mm$, the NO profiles of F1 and F1-Inst are almost identical with a mild difference between the flame branches as noticed in radial profiles (Fig. 16).

As discussed earlier in Sec. 3.1, NO data beyond $z > 60\ mm$ is susceptible to errors due to intense soot-LII noise. Nevertheless, for relative comparison, we evaluate the NO concentration in sooty regions ($z > 60\ mm$), as shown in Fig. 15c. These profiles can be compared with the mean NO obtained from data conditioned on instantaneous B2 branch (plotted in Fig. 17). Such evaluation does not require detuned subtraction (detailed subsequently), and thus, serves as a reference to assess the accuracy of different approaches. The comparison of Figs. 15c and 17, shows that both the F1 and F1-Inst lead to appreciable error in sooty regions. The detuned subtraction approach relies on the assumption that the interference intensity across tuned and detuned acquisitions remains statistically stationary. However, any drift in experiments (laser wavelength and fluence, camera dark- and shot-noise, flame structure) will void this condition. The PAH-LIF interference is less sensitive to the experimental drifts than the soot-LII interference. Soot can be highly intermittent and localized. The soot-LII response to the laser fluence is highly non-linear. Thus, the mean detuned signal across tuned and detuned campaigns can vary, resulting in erroneous NO concentrations. The NO profiles from F1 and F1-Inst in Fig. 15c diverge when $z > 60\ mm$ despite the same experimental dataset. In the F1 approach, the unmapped mean detuned signal subtraction assumes that the flame is statisti-

cally stationary. Thus, F1 is susceptible to systematic variations of soot and flame branch locations. In the F1-Inst strategy, systematic flame variations are accounted for due to the detuned signal mapping in flame-fixed coordinates. The comparison of Figs. 15c and 17, shows that NO concentration with F1-Inst is less erroneous than that of F1.

Out of the four schemes, the F1-Inst strategy provides better result due to lower interferences and instant-wise mapped PAH subtraction. Therefore, findings of F1-Inst (Fig. 14) are discussed further. The NO concentration along the inner branch B1 remains nearly constant with height (also apparent in Fig. 15a). χ_{NO} varies between 20–30 *ppm*, measuring 25 *ppm* along most of the axial distance. Almost constant χ_{NO} with a residence time (axial distance) and low flame temperature in B1 [2] suggests the formation of NO primarily through non-thermal routes. Recall that B1 is composed of the inner lean-premixed reaction zone (B1-P) and outer adjacent non-premixed reaction zone (B1-D) [2]. As indicated earlier, [7], in the fuel-lean reaction zone B1-P, the nitrous oxide (N_2O) route of NO formation is known to be dominant [40]. The excess air from the products of a fuel-lean flame (B1-P) gets fed into the adjacent non-premixed zone, B1-D. The availability of N_2 from excess air and CH radical from the fuel-rich region (Zone-C) is likely to facilitate NO formation through the Fenimore prompt mechanism in B1-D. Thus, NO observed along the inner B1 branch is likely to be a combination of nitrous oxide (in B1-P) and Fenimore (in B1-D) routes.

The NO concentration along the outer branch (B2) is significantly higher (three times) than that of B1. Unlike B1, no local extinctions are observed in B2. The combustion in B2 takes place largely in the non-premixed mode [2], which generally is stoichiometric. Furthermore, the flow strain near B2 is expected to be lower than in B1. Consequently, the temperature in B2 is found to be higher than that in B1 [2]. At the flame-base, χ_{NO} on B2 measures 35 *ppm* while on B1 it is 30 *ppm*. Since the flow strain is nearly equal at the flame-base, the contrast in χ_{NO} indicate different formation routes in B1 and B2. χ_{NO} along the B2 branch grows from 35 to 75 *ppm* with the residence

time (i.e., z). The appreciable NO growth with the residence time and high temperature in B2 together suggests the formation of NO primarily through the Zeldovich thermal route. In Fig. 14, the NO concentration appears to increase with radial distance until the OH-centerline, and subsequently, χ_{NO} reaches a plateau across B2. The plateau is also evident from the radial profiles in Fig. 16. The NO is spatially biased towards the oxidizer side, instead of being distributed equally on either side of the mean flame-front. This may be due to the availability of nitrogen and oxygen on the oxidizer side of B2.

The axial growth of χ_{NO} along B2 saturates at a certain height (see Fig. 14). The similar observation is noted at a higher height ($z > 60\ mm$) in instantaneous images (Fig. 13). We also deduce the mean χ_{NO} conditioned on the B2 branch from instantaneous images to demonstrate the NO growth saturation conclusively. Recall, the mean χ_{NO} field (Fig. 14) could not be evaluated for $z > 60\ mm$ due to LII interference. Fortunately, in the B2 branch, both the PAH and LII interferences are not significant (see Figs. 8 and 12) with F1 dataset. Thus, χ_{NO} along B2 can be deduced without the need of detuned signal subtraction. The NO-LIF signal within 1.5 mm radial width along B2 is extracted from instantaneous images (such as Fig. 13a). The values are averaged in the radial direction to deduce a spatially-averaged axial χ_{NO} profile. Such instantaneous profiles are conditionally (at least 200 samples) averaged over 1500 instants. The resulting mean χ_{NO} evolution along B2 is shown in Fig. 17 until $z = 76\ mm$.

The NO growth saturates at $z \approx 60\ mm$. Radiation from soot particles can lower the flame temperature, consequently decelerating the NO growth. In the sooting region ($z > 60\ mm$), NO concentration even decreases by ~15% between $z = 60$–$76\ mm$. As discussed in Sec. 3.3.6, the mean soot concentration values listed in Table 2 may reduce the flame temperature by 50 K. Even this small drop in temperature could alter the NO concentration drastically. For instance, a 50–70 K drop was shown to reduce χ_{NO} by 20–25% [37, 41]. The net reduction in χ_{NO} is a balance between the reduced NO formation rate and NO diffusion/dilution processes in downstream regions. Thus, for accurate NO

predictions, radiation heat losses from soot particles must be considered.

4. Conclusions

Quantitative instantaneous and mean NO mole fractions are evaluated in the n-heptane jet spray flame using NO-LIF. The LIF temperature-quenching sensitivity is reduced through the optimized $Q_1(29.5)$ excitation [7]. This optimization is achieved by simulating the LIF signal for different excitation schemes. Temperature and gas composition needed for the LIF simulations are obtained from the spray flame LES data. The LIF model and LES data are also used to incorporate the temperature-quenching LIF correction in the spray flame.

To reduce PAH and soot interferences, the NO-LIF detection strategy is optimized by imaging LIF in different spectral ranges, namely broadband (F6), intermediate (F3) and narrowband (F1). F6 results in significant interference due to broadband detection. To minimize LII interferences in sooting regions, lower laser fluence and narrower spectral collection with high detection efficiency are recommended.

The F1 detection showed the least interference, and thus, it is used to evaluate the instantaneous χ_{NO}. A novel approach of instant-wise mapped PAH subtraction is introduced using the NO-detuned signal mapped to flame-fixed coordinates. Various insights are derived from the instantaneous NO distribution in the complex (local extinctions, PAH, and sooting regions) spray flame. The conditional mean χ_{NO} is also evaluated from the instant-wise PAH subtracted fields (F1-Inst), which is compared with F6, F3, and F1. The uncertainty in mean χ_{NO} is estimated to be $\pm 30\%$, while instantaneous χ_{NO} is accurate only within $\pm 75\%$ due to photon shot-noise. The shot-noise in instantaneous χ_{NO} is reduced by area-averaging (size $> 0.3\ mm$), reducing the uncertainty to only $\pm 33\%$ which is reasonable to obtain instantaneous χ_{NO}.

Instantaneous NO concentration fields indicate that the small-scale ($< 1\ mm$) extinctions do not affect the NO. However, the large-scale extinctions sharply reduce the NO concentration, most likely due to reduced temperature. A typ-

ical reduction of 80% in local χ_{NO} is observed. Instantaneous images near sooting regions show a decrease in PAH intensity and spatial distribution since the smaller PAH get converted to larger PAH that eventually produce soot. Similarly, OH concentrations are observed to diminish significantly in the presence of soot due to a dominant role of OH in soot oxidation reactions. The NO concentration along the outer branch (B2) increases up to $z = 60\ mm$, beyond which the NO growth decelerates, eventually leading to 15% reduction in NO at $z = 76\ mm$. This is due to a possible decrease in flame temperature owing to the radiation from soot particles.

The mean χ_{NO} showed nearly identical spatial distribution as of [7], although values differed slightly. Nevertheless, the differences between all four detections (F6, F3, F1, F1-Inst) are within the uncertainty (i.e., $\pm 30\%$). F1-Inst data is the most reliable due to the narrowband detection and mapped PAH subtraction. This strategy provided access to χ_{NO} even near sooting regions ($z > 60\ mm$). The fuel droplet and flame interaction lead to the formation of composite reaction zones. Consequently, NO in the spray flame forms through different mechanisms. The mean χ_{NO} along the inner composite branch (B1) is nearly constant ($20 - 30\ ppm$) with height, suggesting non-thermal routes of NO formation. In B1-P (lean-premixed), nitrous oxide route could be prevalent, while in B1-D (diffusion) prompt route of NO formation is likely. A region of low NO in the vicinity of B1 is attributed to local extinctions, as confirmed by instantaneous NO fields. In the outer diffusion branch B2, the thermal mechanism of NO formation appears to be dominant as evidenced by the NO growth. χ_{NO} along $B2$, increases from 35 ppm at the flame-base to 75 ppm at $z = 60\ mm$.

The present work contributes to the spray combustion field on the following three aspects, *i*) NO measurement and data reduction strategies, *ii*) database enhancement of mean NO concentration, and *iii*) understanding of effects of local flame extinctions, soot radiation, and combustion mode on NO through instantaneous and mean quantitative imaging of NO concentration.

Acknowledgments

The authors are grateful for the financial support of Safran Aircraft Engines and the French National Research Agency (Industrial chair PERCEVAL, ANR-15-CHIN-0001). The assistance of Mr. A. Vandel in setting-up the burner is gratefully acknowledged.

Table 1: Detuned to tuned signal ratio at $z = 42\ mm$.

$\bar{c}$	Detuned/Tuned (%)		
	F6	F3	F1
1	54	51	44
0.9	38	13	10
0.3	27	13	9

Table 2: Soot volume fraction statistics from [36] at radial maxima.

$z\ (mm)$	$\langle f_v \rangle$	σ_{f_v}	$\langle f_v \rangle_c$
60	0.06	0.08	0.26
76	0.15	0.18	0.30

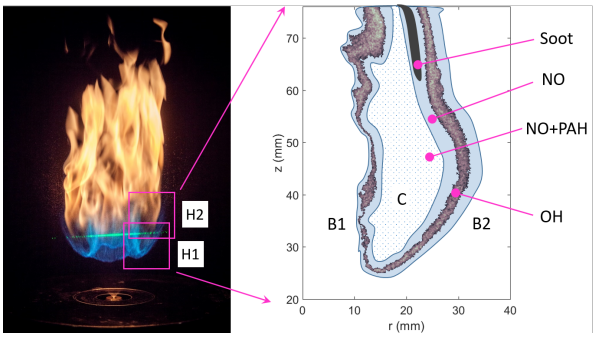

Figure 1: Flame photograph with view fields (H1 and H2) and the schematic illustrating the expected regions of NO, PAH, and soot along with the OH-PLIF signal.

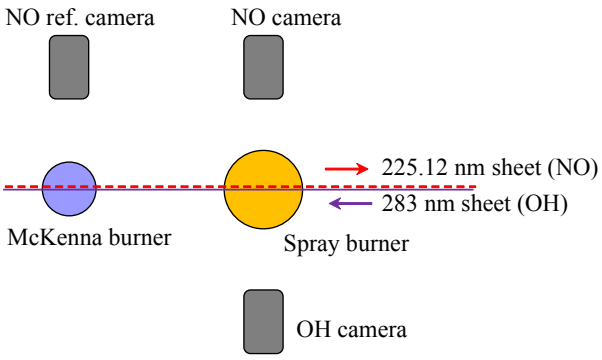

Figure 2: Laser diagnostics set-up.

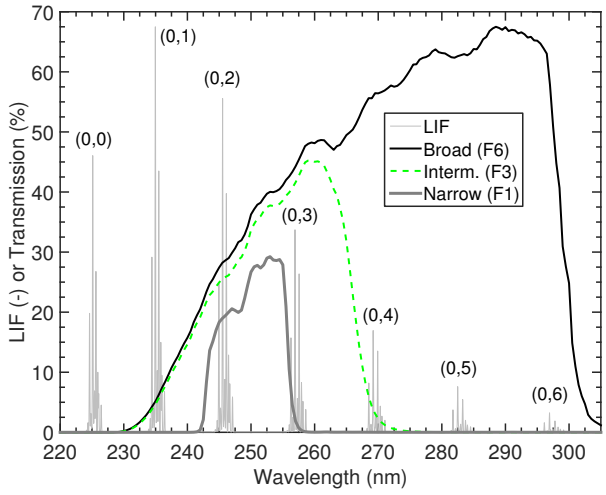

Figure 3: NO-LIF filter transmission along with the normalized NO fluorescence spectrum. Spectrum is simulated in synthetic air at an atmospheric pressure using a CORIA LIF model [7, 23]. $(0,0)$–$(0,6)$ denote the NO fluorescence bands of A–X excitation.

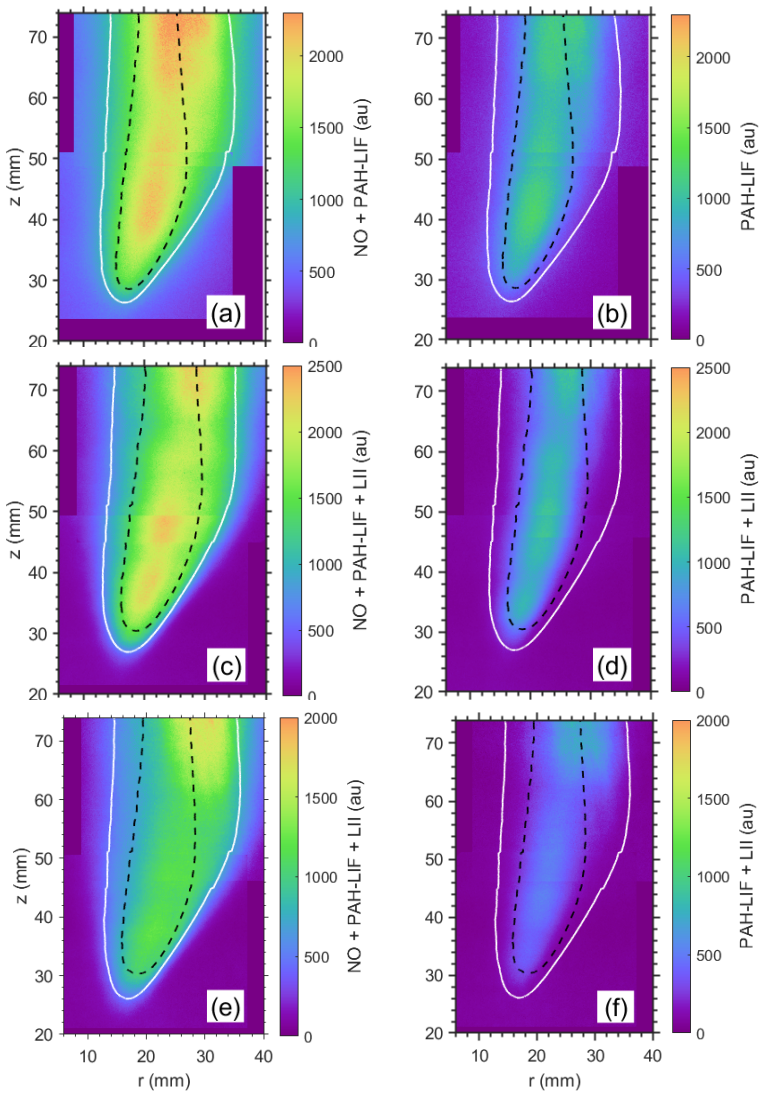

Figure 4: Mean (unconditional) LIF signal tuned to NO transition at 225.12 nm: (a) F6, (c), F3 (e) F1, and corresponding detuned signal: (b) F6, (d), F3 (f) F1, along with the mean flame-front $\bar{c} = 0.3$ (solid white) and 0.9 (dashed black).

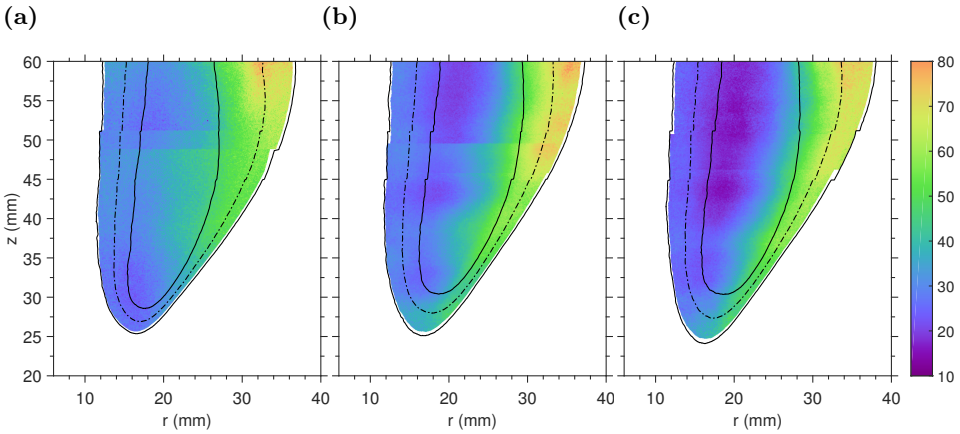

Figure 5: Conditionally averaged χ_{NO} (in *ppm*): (a) F6, (b) F3, and (c) F1, along with $\bar{c}$ contours of 0.1 (outer), 0.5, and 0.9 (inner).

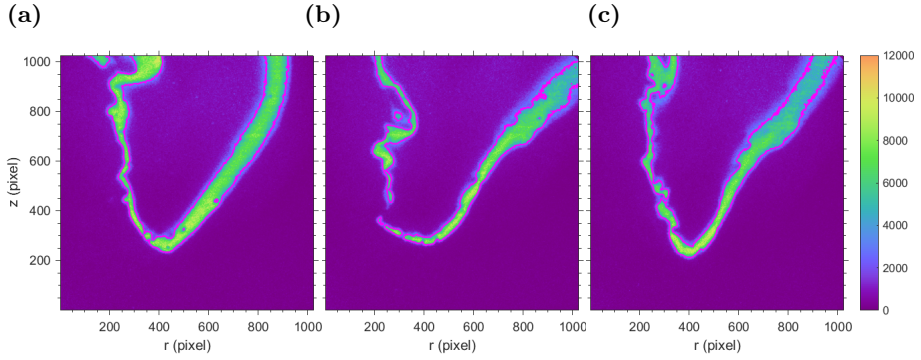

Figure 6: Instantaneous OH-PLIF signal (*au*) with isocontour (3500 *counts*) at H1.

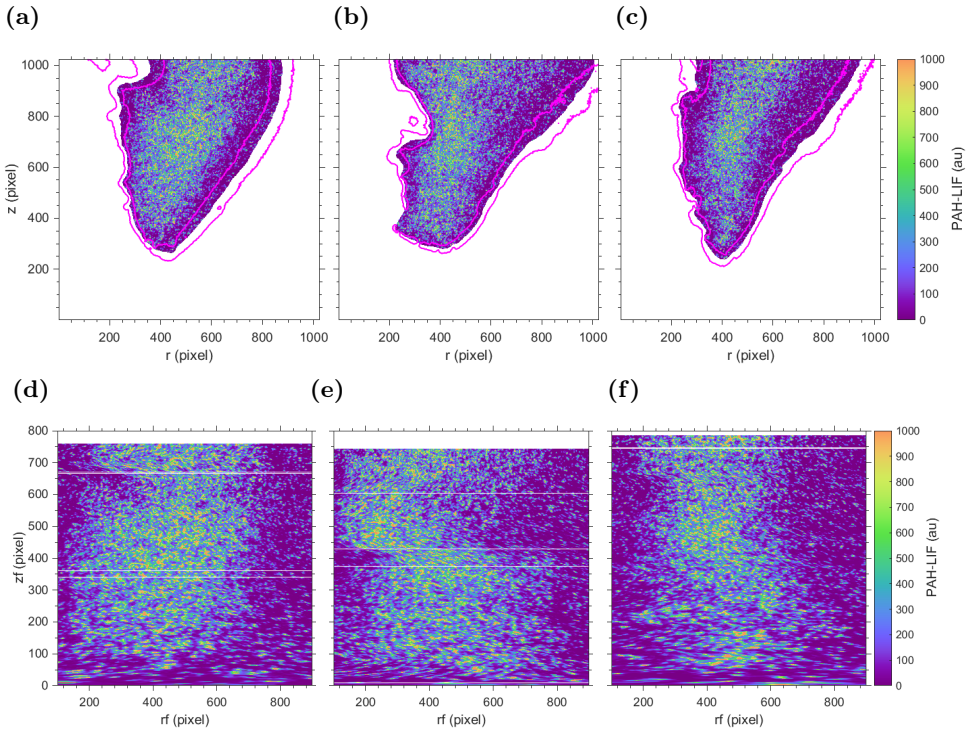

Figure 7: PAH mapping at H1: (a-c) Instantaneous detuned LIF signal (PAH) with OH isocontours, (d-f) PAH mapping to inner and outer flame branches with flame-fixed coordinates.

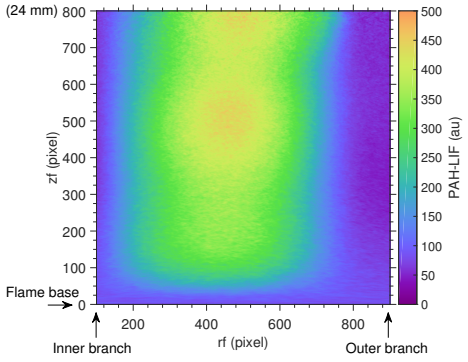

Figure 8: Mean PAH map at H1.

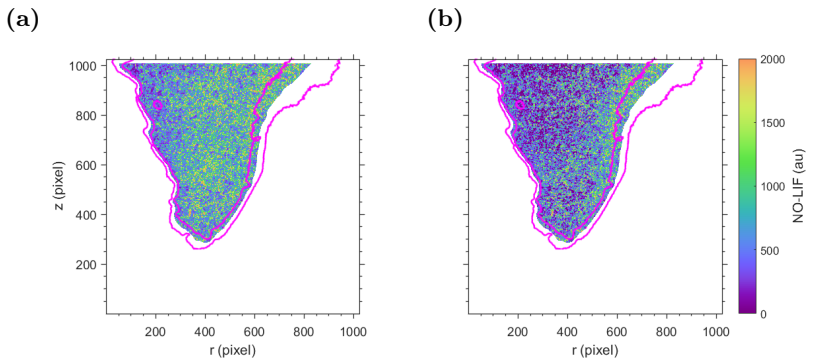

Figure 9: Instant-wise PAH subtraction: (a) instantaneous NO (+ PAH) LIF, (b) PAH subtracted NO-LIF.

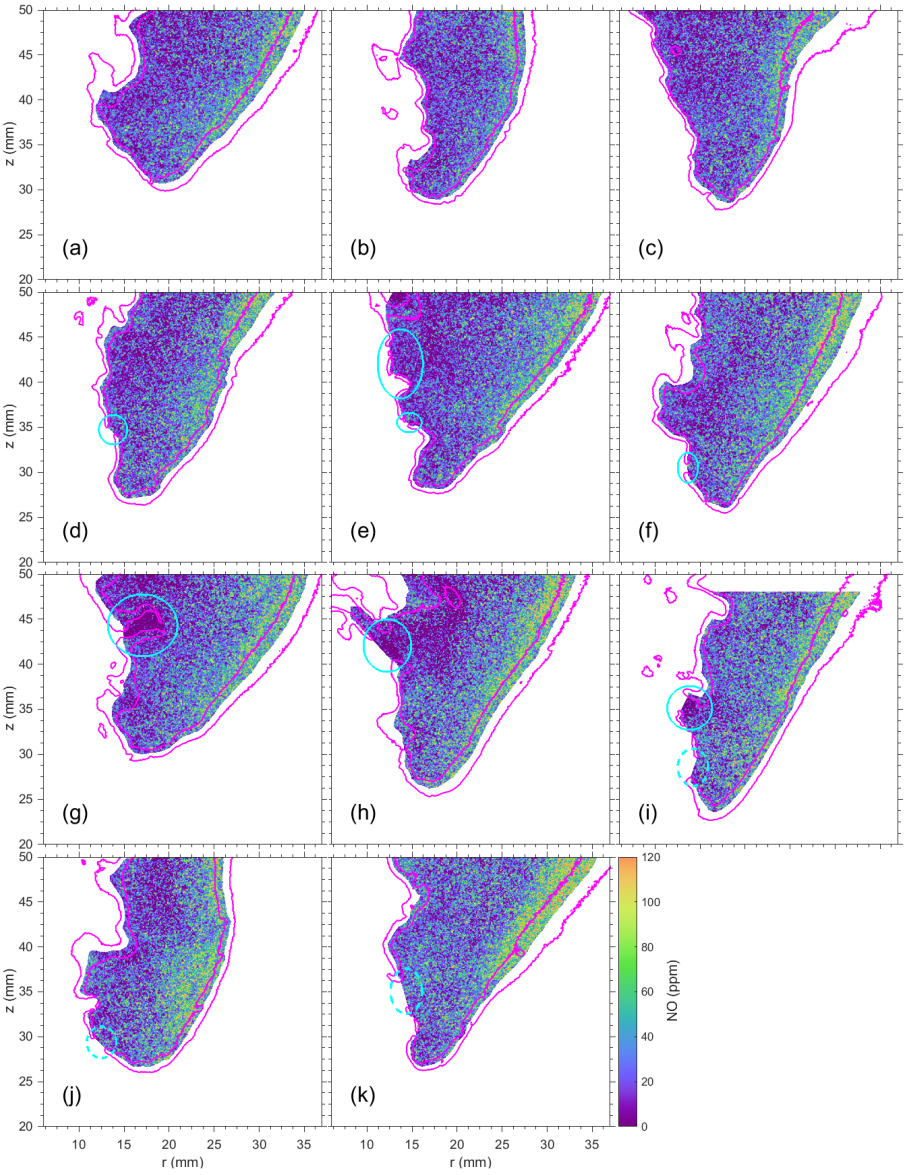

Figure 10: Instantaneous NO concentration at H1: (a-c) without local flame extinction, (d-f) with small-scale ($< 1\ mm$) extinction, (g-i) large-scale extinction with negligible NO regions, (i-k) large-scale extinction yet non-negligible NO concentrations. The OH isocontours are marked in magenta, while the extinction regions are highlighted by ellipses in cyan.

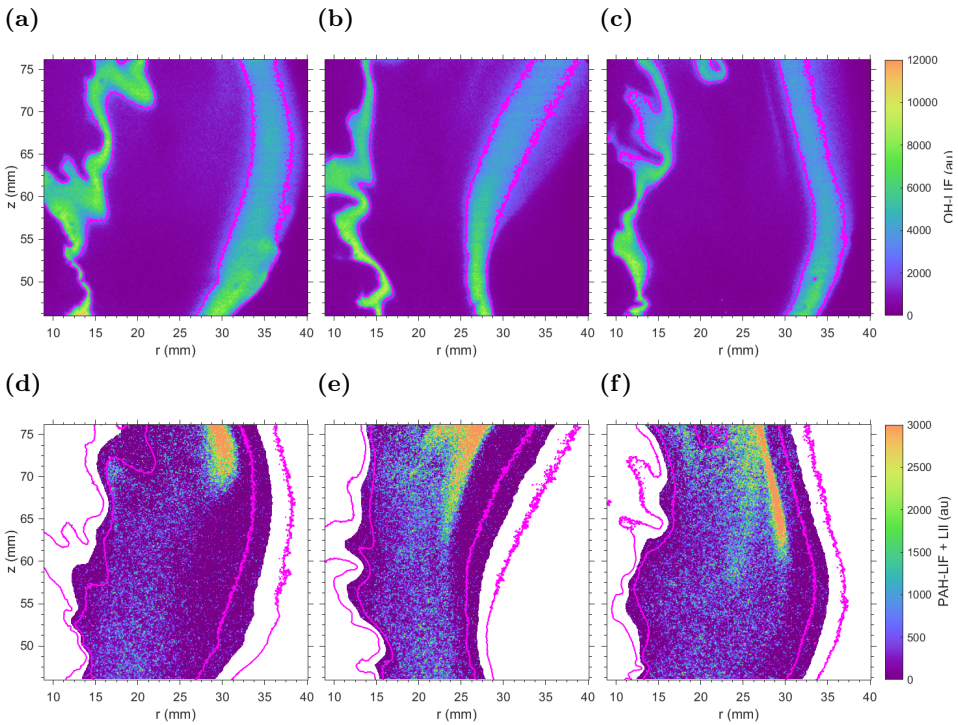

Figure 11: PAH and LII interferences at H2, (a-c): instantaneous OH-PLIF with isocontour (2500 *counts*), (d-f): instantaneous detuned signal (PAH-LIF + soot-LII) with OH isocontour.

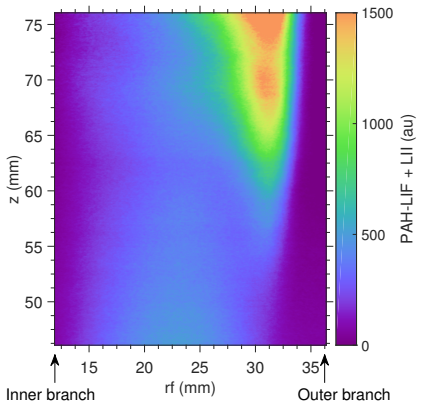

Figure 12: Mean PAH-LII map at H2.

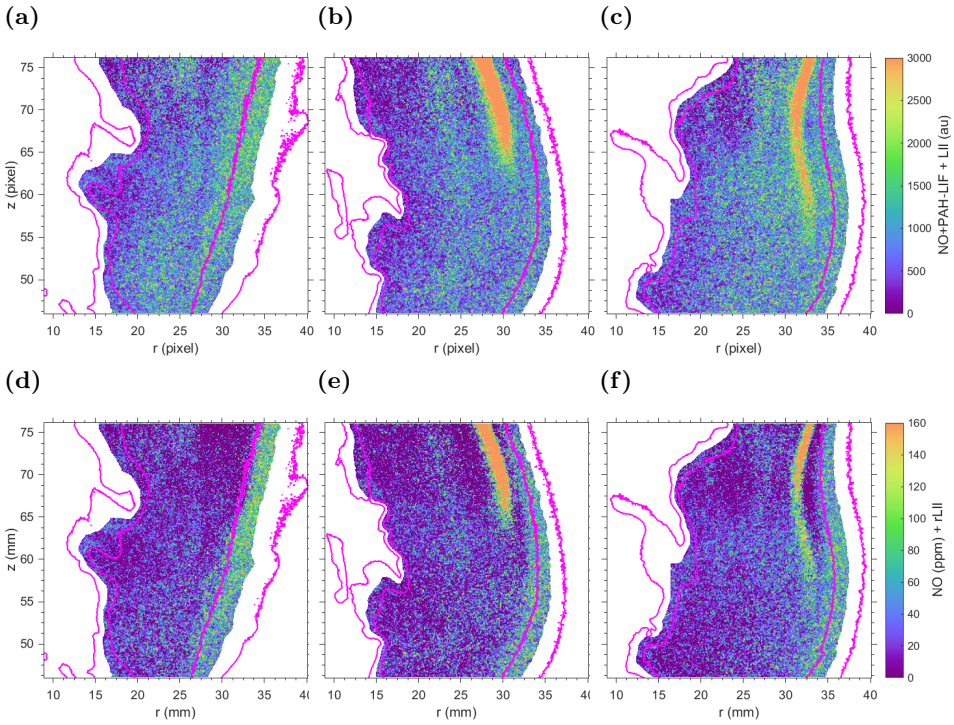

Figure 13: Instantaneous NO concentration at H2: (a-c) tuned signal containing NO, PAH, LII contribution, (d-f) NO concentration in *ppm* valid along the entire height of B1 and B2 branches (within OH-layer). The data within the region bounded by B1 and B2 branches (Zone-C) is valid only below $z = 60\ mm$.

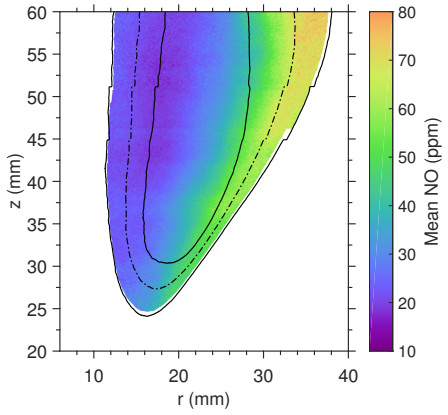

Figure 14: Conditionally averaged χ_{NO} based on instant-wise PAH subtraction (F1-Inst), along with $\bar{c}$ contours of 0.1 (outer), 0.5, and 0.9 (inner).

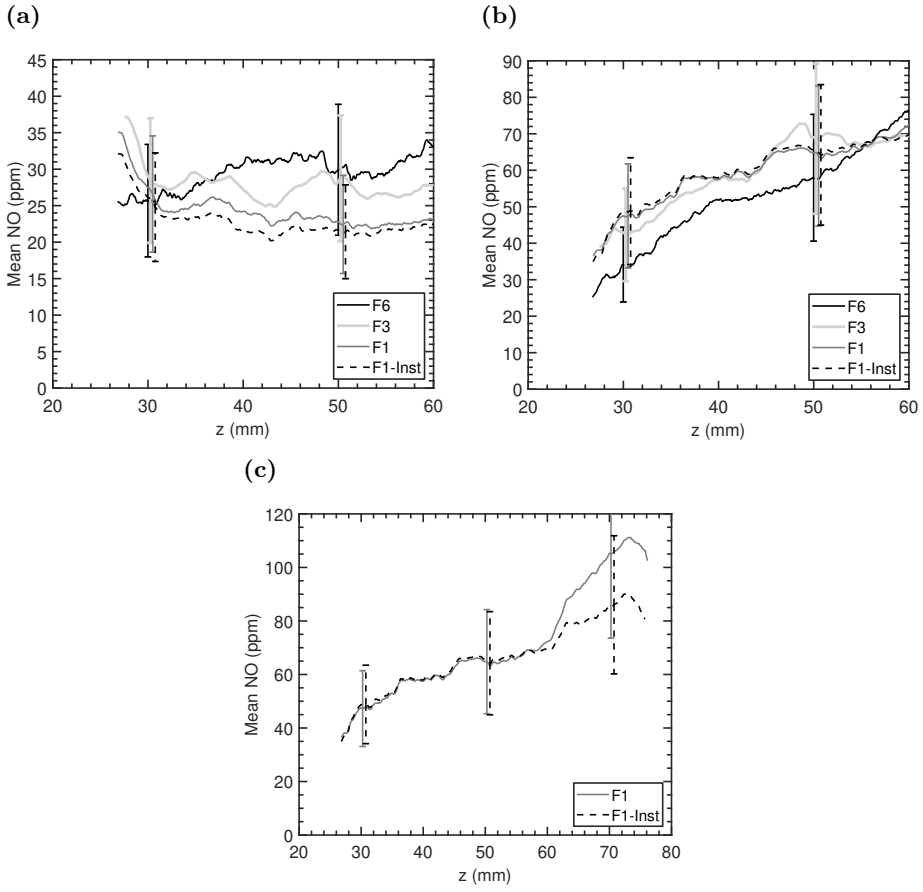

Figure 15: Mean NO concentration axial profiles along: (a) B1 branch, (b) B2 branch, with various strategies (F6, F3, F1, F1-Inst), (c) B2 branch for $z > 60\ mm$.

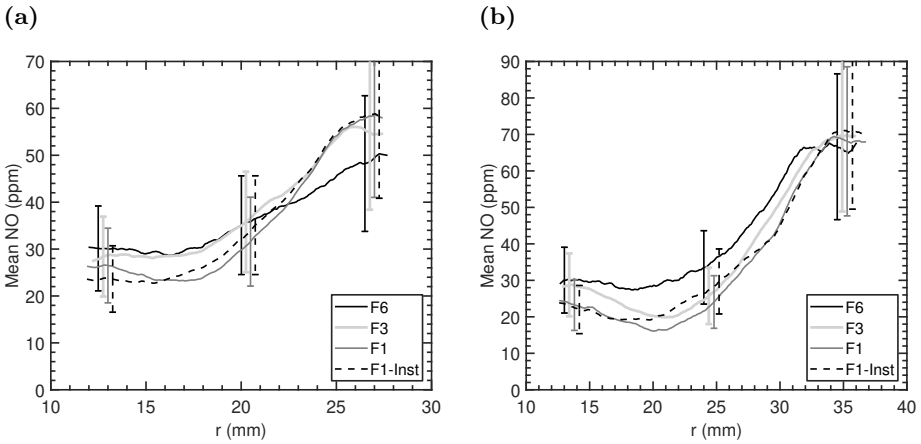

Figure 16: Mean NO concentration radial profiles with various strategies (F6, F3, F1, F1-Inst) at: (a) $z = 38\ mm$ (b) $z = 55\ mm$.

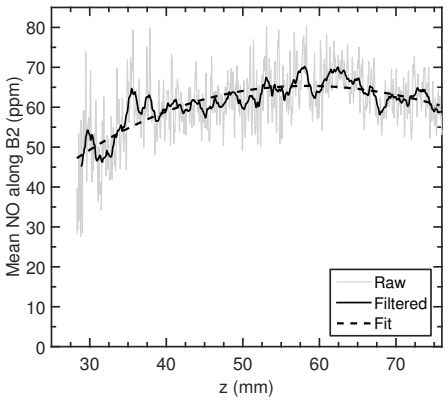

Figure 17: Mean χ_{NO} conditioned on B2 branch.

Appendix A. Filter transmission

Table A.3: Filter transmission at NO-LIF bands (refer Fig. 3 of the paper) for each detection.

Wavelength (nm)	Transmission (%)		
	F6 (Broad)	F3 (Interm.)	F1 (Narrow)
225	2.1e-12	1.5e-12	4.2e-18
235	5	5	2.7e-06
245	27	25	18
257	44	42	2
269	55	4	1.3e-02
282	62	2.1e-02	5.2e-03
297	58	3.9e-03	1.9e-03

Appendix B. Data processing steps

Appendix B.1. Flame-front and progress variable from OH-PLIF

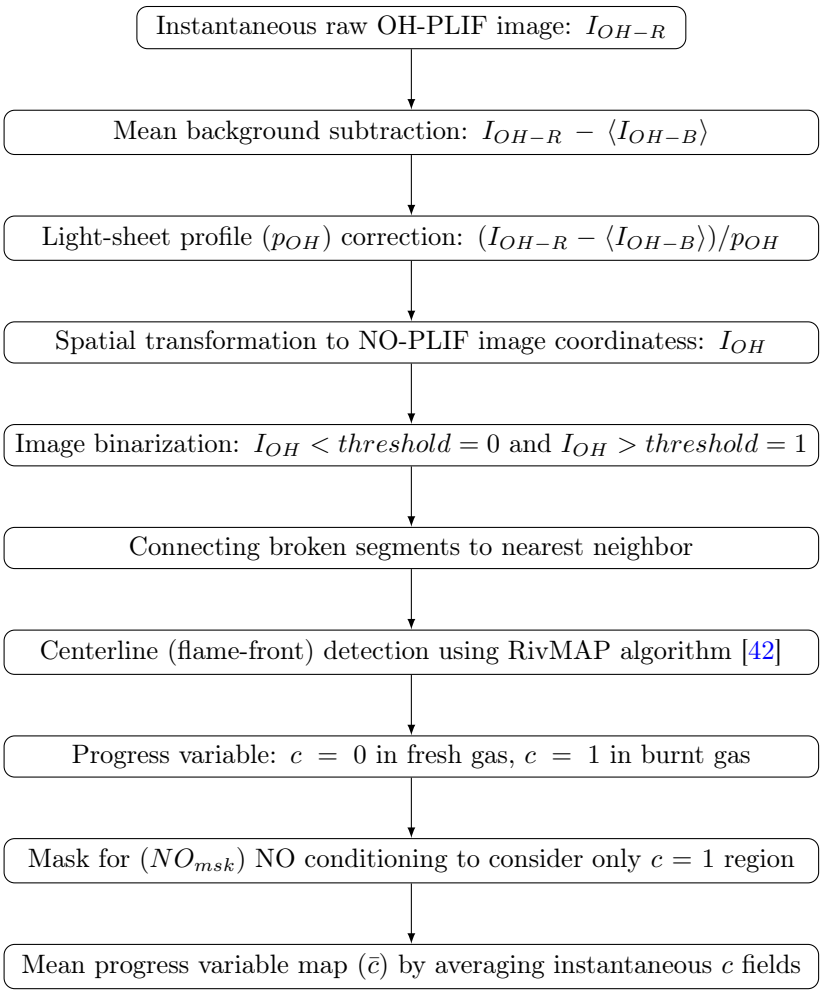

Figure B.18: Flame-front detection steps.

Appendix B.2. NO calibration deduction steps

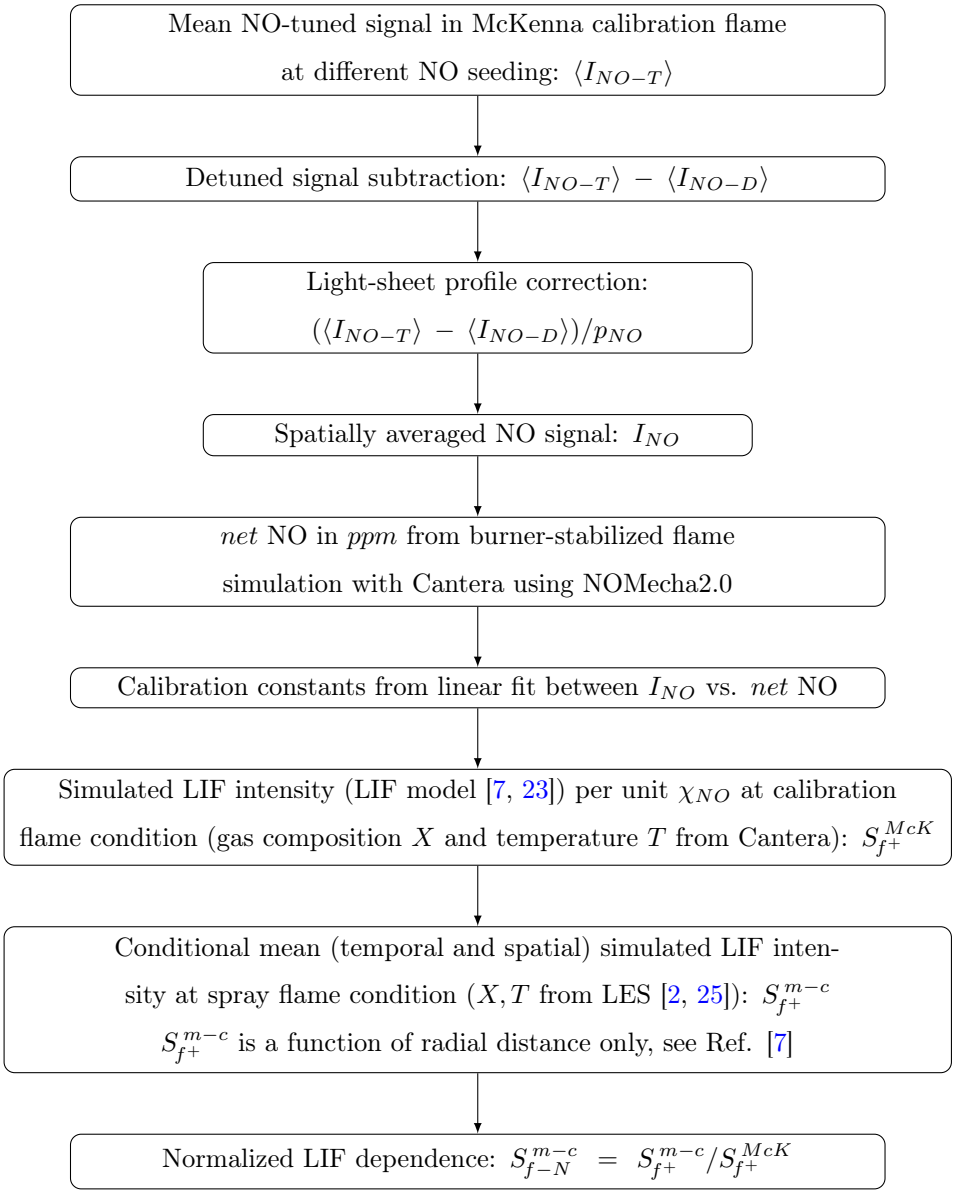

Figure B.19: NO calibration deduction procedure.

Appendix B.3. Mean NO in spray flame for F6, F3, and F1 dataset

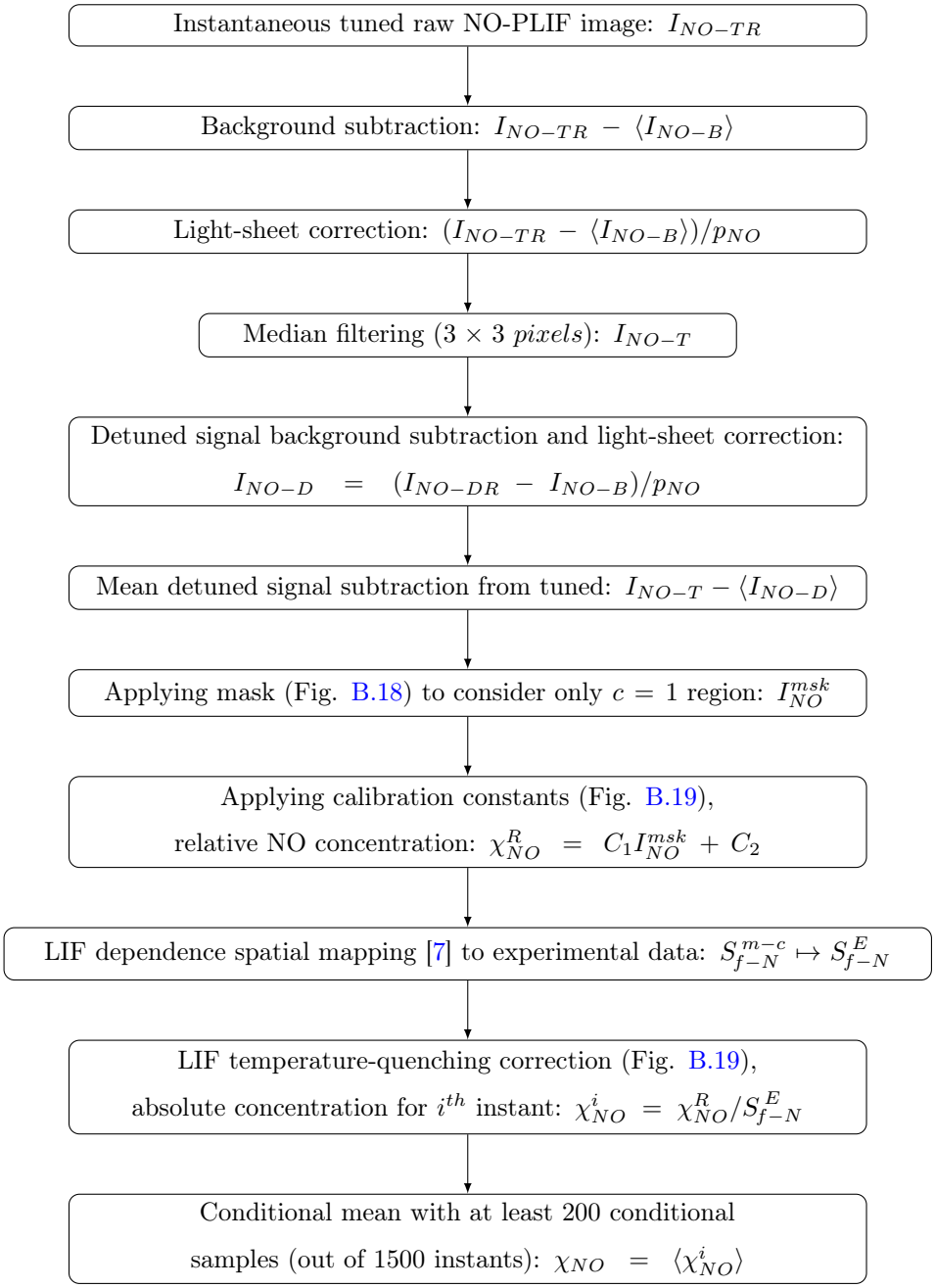

Figure B.20: Data processing to obtain Conditionally averaged NO concentration.

Appendix B.4. PAH mapping in spray flame for F1 dataset

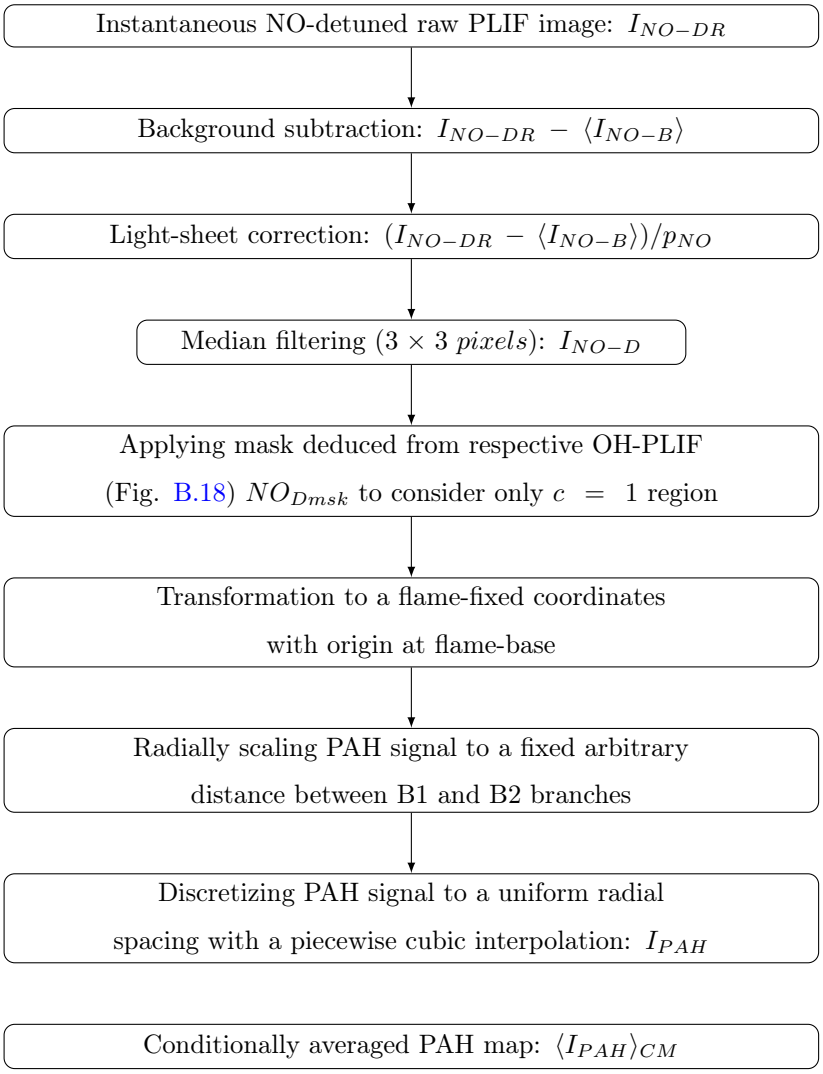

Figure B.21: PAH mapping procedure.

Appendix B.5. Instantaneous NO concentration in spray flame from F1 dataset

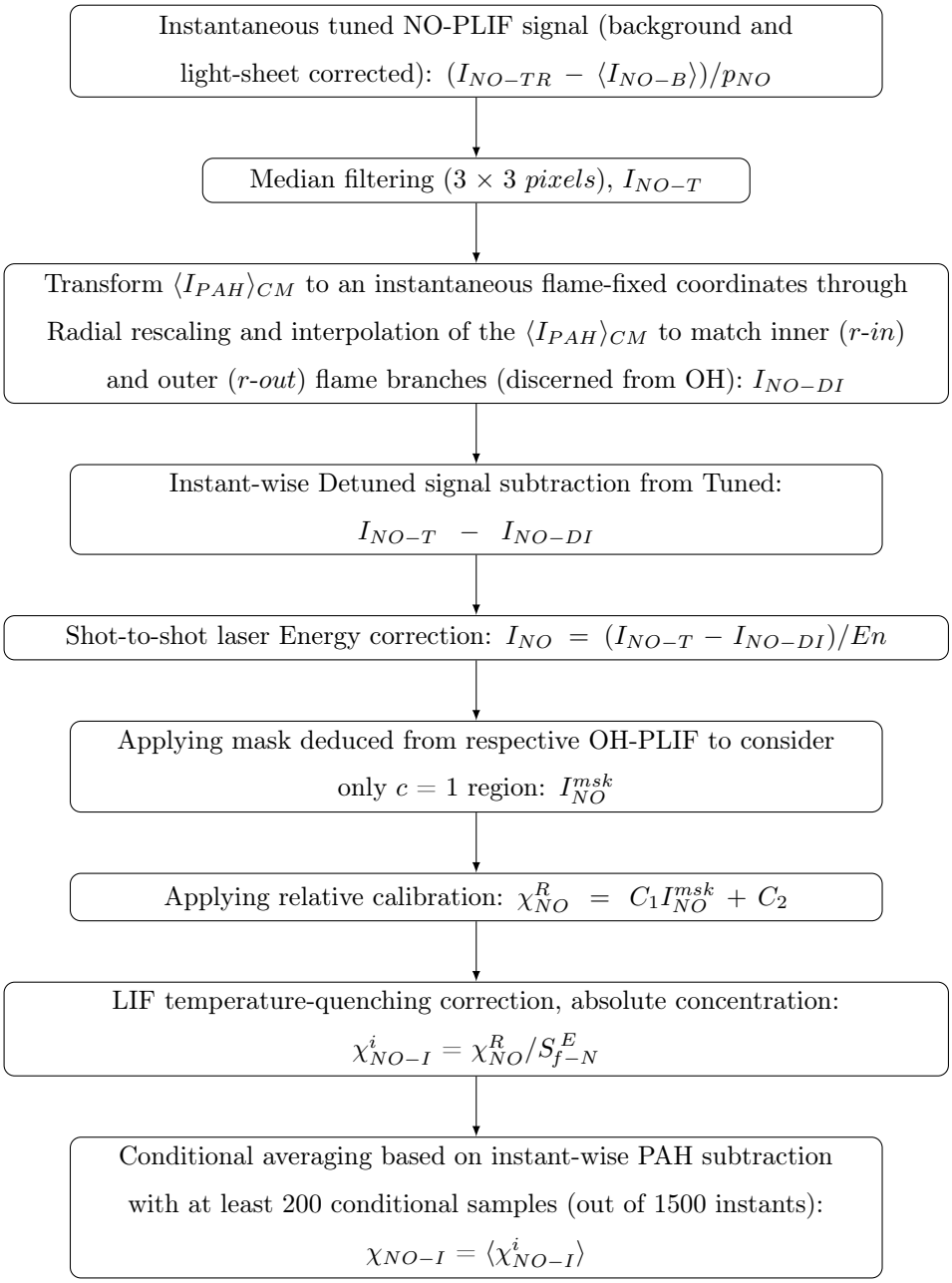

Figure B.22: Instantaneous NO concentration deduction.

Appendix C. NO-LIF Calibration

Appendix C.1. Calibration in McKenna burner

The measurement and data processing protocols to calibrate the NO-LIF signal are identical as of [7]. The data reduction steps are also provided in Appendix B.2. The NO-seeded methane/air flames ($\phi = 0.8$) were stabilized on a water-cooled McKenna burner. The *net* NO concentration is defined as *nascent* + *seeded* − *consumed*, where the flame generated NO is referred to as *nascent*, the NO re-burned is called as *consumed*. To calculate the *net* NO, burner stabilized non-adiabatic flame simulations were performed, as detailed in [7]. To verify interferences (other than soot and PAH), the LIF signal was also acquired by detuning the laser to off-NO transition at 225.386 *nm* (specified in a vacuum). A total of 200 images were acquired for both the tuned and detuned experiments. The time-averaged detuned signal was subtracted from the $Q_1(29.5)$ transition-tuned mean LIF signal. Figure C.23a shows the spatially-averaged NO-LIF signal (detuned-subtracted) as a function of *net* NO for F3 and F1. Excellent linearity is observed between the NO concentration and LIF signal. The calibration coefficients are derived from the least-square linear fit.

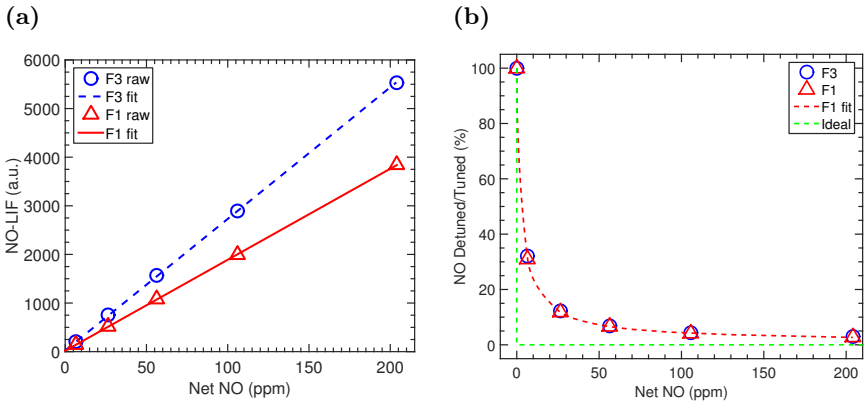

Figure C.23: NO-LIF calibration in McKenna burner-stabilized flames: (a) LIF signal intensity (*tuned* − *detuned*) with *net* NO, (b) Detuned to tuned signal ratio.

Figure C.23b shows the tuned to detuned LIF ratio along with an ideal curve. In ideal (interference-free) scenario, the detuned and tuned signals would be equal in a gas without any NO, and thus, the ratio is unity. For a finite NO concentration, detuned to tuned ratio should approach zero, as shown by the ideal curve in Fig. C.23b. However, interferences do exist in the measurement. The measured trend approaches the ideal curve at higher NO concentrations. The detuned signal contribution drops asymptotically with NO concentration, and accounts to only 2.7% at 200 *ppm* of NO. The ratios are almost identical with F3 and F1.

Appendix C.2. Tuned and detuned NO-LIF signals with F1

The detuned signal contribution amounts to 2.7% at 200 *ppm* of NO with F1, as noted above. To investigate further, tuned and detuned LIF signal intensities are plotted separately in Fig. C.24. Although negligible, the detuned signal

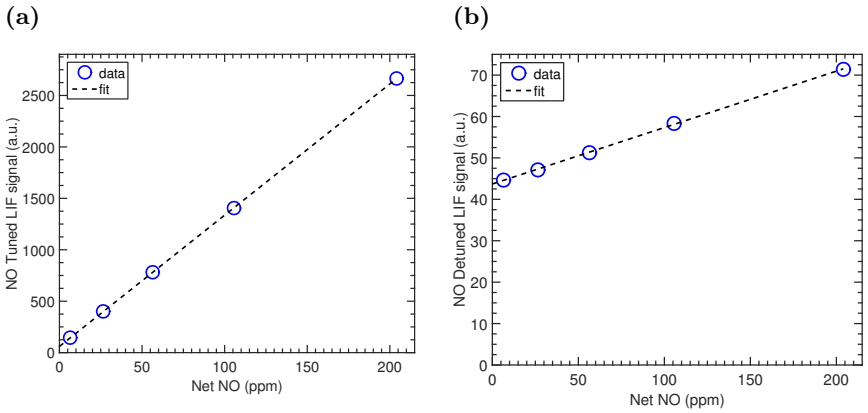

Figure C.24: NO tuned (a) and detuned (b) LIF signals in McKenna calibration flames as a function of net NO concentration.

in Fig. C.24b shows a finite value (44 counts) at *net* NO concentration of 0 *ppm*, which suggests a weak interference, perhaps from O_2 or CO_2. Since the calibration flame is fuel-lean, PAH fluorescence is not expected. The detuned signal in Fig. C.24b increases negligibly but linearly with NO concentration, which suggests a weak excitation of NO. The detuned signal measured 44 and

71 counts at *net* NO of 0 and 200 *ppm*, respectively. Therefore, weak NO excitation contribution is 27 counts, while non-NO contribution is 44 counts. Consequently, 2.7% of detuned contribution at 200 *ppm* is composed of 1% NO-LIF (weak excitation) and 1.7% interference from other species. This minor interference is accounted for through the calibration procedure since the detuned signal is subtracted (in Fig. C.23a) and the same detuned-subtraction protocol was applied to the spray flame data reduction.

Appendix D. Mean NO profiles (unfiltered)

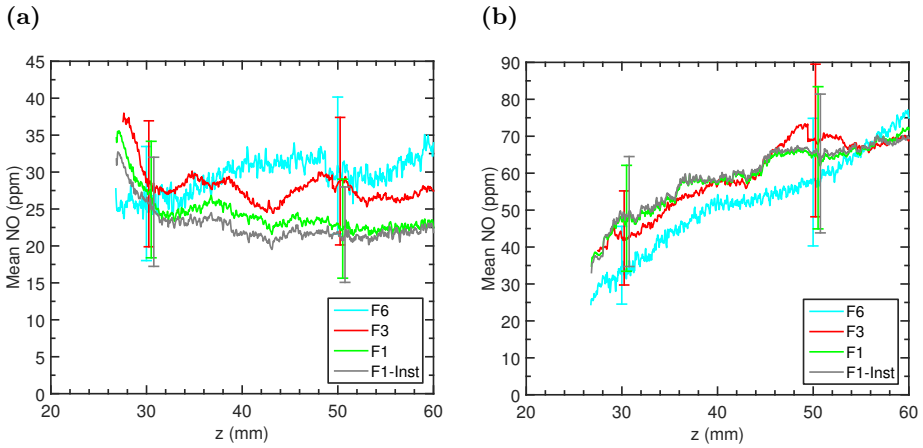

Figure D.25: Mean (unfiltered) NO concentration axial profiles along: (a) B1 branch (b) B2 branch, with various strategies (F6, F3, F1, F1-Inst). The corresponding filtered profiles are shown in Fig. 15.

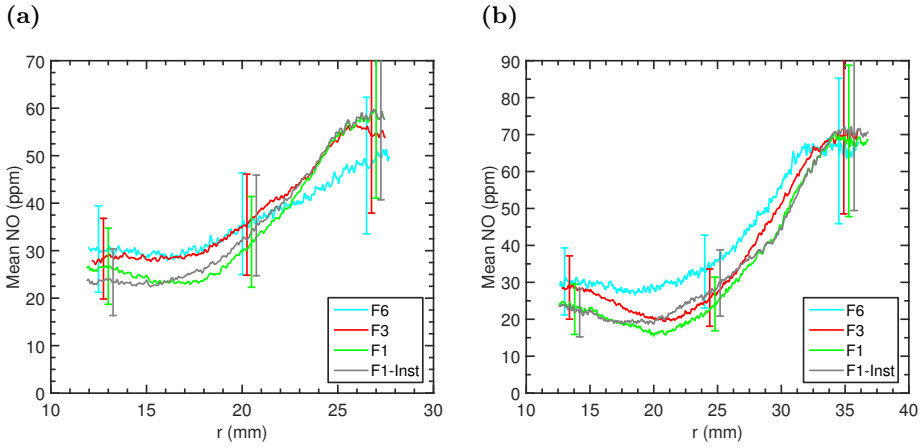

Figure D.26: Mean (unfiltered) NO concentration radial profiles with various strategies (F6, F3, F1, F1-Inst) at: (a) $z = 38\ mm$ (b) $z = 55\ mm$. The corresponding filtered profiles are shown in Fig. 16.

References

[1] A. Verdier, J. M. Santiago, A. Vandel, G. Godard, G. Cabot, B. Renou, Local extinction mechanisms analysis of spray jet flame using high speed diagnostics, Combust. Flame 193 (2018) 440–452. doi:10.1016/j.combustflame.2018.03.032.

[2] F. Shum-Kivan, J. M. Santiago, A. Verdier, E. Riber, B. Renou, G. Cabot, B. Cuenot, Experimental and numerical analysis of a turbulent spray flame structure, Proc. Combust. Inst. 36 (2017) 2567–2575. doi:10.1016/j.proci.2016.06.039.

[3] 6th workshop on measurement and computation of turbulent spray combustion, http://www.tcs-workshop.org/tcs6.html (Accessed on 2019-07-08).

[4] J. D. Gounder, A. Kourmatzis, A. R. Masri, Turbulent piloted dilute spray flames: Flow fields and droplet dynamics, Combust. Flame 159 (11) (2012) 3372–3397. doi:10.1016/j.combustflame.2012.07.014.

[5] R. Yuan, J. Kariuki, A. Dowlut, R. Balachandran, E. Mastorakos, Reaction zone visualisation in swirling spray n -heptane flames, Proc. Combust. Inst. 35 (2) (2015) 1649–1656. doi:10.1016/j.proci.2014.06.012.

[6] A. Verdier, J. M. Santiago, A. Vandel, S. Saengkaew, G. Cabot, G. Grehan, B. Renou, Experimental study of local flame structures and fuel droplet properties of a spray jet flame, Proc. Combust. Inst. 36 (2017) 2595–2602. doi:10.1016/j.proci.2016.07.016.

[7] I. A. Mulla, G. Godard, G. Cabot, F. Grisch, B. Renou, Quantitative imaging of nitric oxide concentration in a turbulent n-heptane spray flame, Combust. Flame 203 (2019) 217–229. doi:10.1016/j.combustflame.2019.02.005.

[8] A. B. Sahu, R. V. Ravikrishna, Quantitative LIF measurements and kinetics assessment of NO formation in H_2/CO syngas-air counterflow diffusion flames, Combust. Flame 173 (2016) 208–228. doi:10.1016/j.combustflame.2016.09.003.

[9] Z. Wang, Y. Zhou, R. Whiddon, Y. He, K. Cen, Z. Li, Investigation of NO formation in premixed adiabatic laminar flames of H_2/CO syngas and air by saturated laser-induced fluorescence and kinetic modeling, Combust. Flame 164 (2016) 283–293. doi:10.1016/j.combustflame.2015.11.027.

[10] T. Lee, J. B. Jeffries, R. K. Hanson, Experimental evaluation of strategies for quantitative laser-induced-fluorescence imaging of nitric oxide in high-pressure flames (1–60 bar), Proc. Combust. Inst. 31 (2007) 757–764. doi:10.1016/j.proci.2006.07.090.

[11] J. Yoo, T. Lee, J. B. Jeffries, R. K. Hanson, Detection of trace nitric oxide concentrations using 1-D laser-induced fluorescence imaging, Appl. Phys. B 91 (3) (2008) 661–667. doi:10.1007/s00340-008-3030-6.

[12] R. Ravikrishna, S. V. Naik, C. S. Cooper, N. M. Laurendeau, Quantitative laser-induced fluorescence measurements and modeling of nitric oxide in high-pressure (6–15 atm) counterflow diffusion flames, Combust. Sci. Technol. 176 (1) (2004) 1–21. doi:10.1080/00102200490267331.

[13] K. Verbiezen, R. Klein-Douwel, A. van Vliet, A. Donkerbroek, W. Meerts, N. Dam, J. ter Meulen, Quantitative laser-induced fluorescence measurements of nitric oxide in a heavy-duty diesel engine, Proc. Combust. Inst. 31 (1) (2007) 765–773. doi:10.1016/j.proci.2006.07.061.

[14] W. G. Bessler, M. Hofmann, F. Zimmermann, G. Suck, J. Jakobs, S. Nicklitzsch, T. Lee, J. Wolfrum, C. Schulz, Quantitative in-cylinder NO-LIF imaging in a realistic gasoline engine with spray-guided direct injection, Proc. Combust. Inst. 30 (2) (2005) 2667–2674. doi:10.1016/j.proci.2004.08.123.

[15] U. Fissenewert, V. Sick, H. Pucher, Characterization of combustion and NO formation in a spray-guided gasoline direct-injection engine using chemiluminescence imaging, NO-PLIF, and fast NO exhaust gas analysis, in: SAE Technical Paper Series, SAE International, 2005. doi:10.4271/2005-01-2089.

[16] G. Suck, J. Jakobs, S. Nicklitzsch, T. Lee, W. G. Bessler, M. Hofmann, F. Zimmermann, C. Schulz, NO laser-induced fluorescence imaging in the combustion chamber of a spray-guided direct-injection gasoline engine, in: SAE Technical Paper Series, SAE International, 2004. doi:10.4271/2004-01-1918.

[17] K. Verbiezen, R. Klein-Douwel, A. van Vliet, A. Donkerbroek, W. Meerts, N. Dam, J. ter Meulen, Attenuation corrections for in-cylinder NO LIF measurements in a heavy-duty Diesel engine, App. Phy. B 83 (1) (2006) 155–166. doi:10.1007/s00340-006-2141-1.

[18] T. Ottenwälder, C. Schulz, T. Raffius, H.-J. Koß, G. Grünefeld, K. A. Heufer, S. Pischinger, Quantitative nitrogen oxide measurements by laser-induced fluorescence in diesel-like n-heptane jets with enhanced premixing, Combust. Flame 188 (2018) 250–261. doi:10.1016/j.combustflame.2017.09.035.

[19] C. S. Cooper, N. M. Laurendeau, Quantitative measurements of nitric oxide in high-pressure (2–5 atm), swirl-stabilized spray flames via laser-induced fluorescence, Combust. Flame 123 (1-2) (2000) 175–188. doi:10.1016/S0010-2180(00)00165-6.

[20] C. S. Cooper, R. V. Ravikrishna, N. M. Laurendeau, Comparisons of laser-saturated, laser-induced, and planar laser-induced fluorescence measurements of nitric oxide in a lean direct-injection spray flame, Appl. Opt. 37 (21) (1998) 4823–4833. doi:10.1364/AO.37.004823.

[21] B. Li, Y. He, Z. Li, A. A. Konnov, Measurements of NO concentration in NH_3-doped CH_4+Air flames using saturated laser-induced fluorescence

and probe sampling, Combust. Flame 160 (1) (2013) 40–46. doi:10.1016/j.combustflame.2012.10.003.

[22] H. Bladh, P.-E. Bengtsson, J. Delhay, Y. Bouvier, E. Therssen, P. Desgroux, Experimental and theoretical comparison of spatially resolved laser-induced incandescence (LII) signals of soot in backward and right-angle configuration, App. Phy. B 83 (3) (2006) 423–433. doi:10.1007/s00340-006-2197-y.

[23] P. Gautier, Dosage des polluants NO et CO par imagerie de fluorescence induite par laser dans les écoulements réactifs, Ph.D. thesis, Normandie Université, France (2017).

[24] W. G. Bessler, C. Schulz, V. Sick, J. W. Daily, A versatile modeling tool for nitric oxide LIF spectra, 3rd Joint Meeting US Sec. Combust. Inst., Chicago, 2003, http://www.lifsim.com (Accessed on 2019-07-08).

[25] F. Shum-Kivan, Simulation des grandes echelles de flammes de spray et modélisation de la combustion non-prémélangée, Ph.D. thesis, Université de Toulouse, France (2017).

[26] M. D. Bohon, T. F. Guiberti, W. L. Roberts, PLIF measurements of non-thermal NO concentrations in alcohol and alkane premixed flames, Combust. Flame 194 (2018) 363–375. doi:10.1016/j.combustflame.2018.05.024.

[27] W. Bessler, C. Schulz, T. Lee, D.-I. Shin, M. Hofmann, J. Jeffries, J. Wolfrum, R. Hanson, Quantitative NO-LIF imaging in high-pressure flames, App. Phy. B 75 (1) (2002) 97–102. doi:10.1007/s00340-002-0946-0.

[28] C. Cooper, N. Laurendeau, Comparison of laser-induced and planar laser-induced fluorescence measurements of nitric oxide in a high-pressure, swirl-stabilized, spray flame, App. Phy. B 70 (6) (2000) 903–910. doi:10.1007/s003400050027.

[29] R. L. V. Wal, K. A. Jensen, M. Y. Choi, Simultaneous laser-induced emission of soot and polycyclic aromatic hydrocarbons within a gas-jet diffusion flame, Combust. Flame 109 (3) (1997) 399–414. doi:10.1016/s0010-2180(96)00189-7.

[30] S. Bejaoui, X. Mercier, P. Desgroux, E. Therssen, Laser induced fluorescence spectroscopy of aromatic species produced in atmospheric sooting flames using UV and visible excitation wavelengths, Combust. Flame 161 (10) (2014) 2479–2491. doi:10.1016/j.combustflame.2014.03.014.

[31] P. Desgroux, X. Mercier, K. A. Thomson, Study of the formation of soot and its precursors in flames using optical diagnostics, Proc. Combust. Inst. 34 (1) (2013) 1713–1738. doi:10.1016/j.proci.2012.09.004.

[32] A. D'Anna, M. Commodo, M. Sirignano, P. Minutolo, R. Pagliara, Particle formation in opposed-flow diffusion flames of ethylene: An experimental and numerical study, Proc. Combust. Inst. 32 (1) (2009) 793–801. doi:10.1016/j.proci.2008.06.200.

[33] D. G. Goodwin, H. K. Moffat, R. L. Speth, Cantera: An object-oriented software toolkit for chemical kinetics, thermodynamics, and transport processes, http://www.cantera.org, version 2.3.0 (2017).

[34] F. Bisetti, G. Blanquart, M. E. Mueller, H. Pitsch, On the formation and early evolution of soot in turbulent nonpremixed flames, Combust. Flame 159 (1) (2012) 317–335. doi:10.1016/j.combustflame.2011.05.021.

[35] P. Singh, C.-J. Sung, PAH formation in counterflow non-premixed flames of butane and butanol isomers, Combust. Flame 170 (2016) 91–110. doi:10.1016/j.combustflame.2016.05.009.

[36] I. Mulla, B. Renou, Simultaneous imaging of soot volume fraction, PAH, and OH in a turbulent n-heptane spray flame, Combust. Flame (2019) Under review, CNF–D–19–00036R1.

[37] A. Beltrame, P. Porshnev, W. Merchan-Merchan, A. Saveliev, A. Fridman, L. Kennedy, O. Petrova, S. Zhdanok, F. Amouri, O. Charon, Soot and NO formation in methane–oxygen enriched diffusion flames, Combust. Flame 124 (1-2) (2001) 295–310. doi:10.1016/s0010-2180(00)00185-1.

[38] R. Puri, R. J. Santoro, K. C. Smyth, The oxidation of soot and carbon monoxide in hydrocarbon diffusion flames, Combust. Flame 97 (2) (1994) 125–144. doi:10.1016/0010-2180(94)90001-9.

[39] H. Guo, P. M. Anderson, P. B. Sunderland, Optimized rate expressions for soot oxidation by OH and O2, Fuel 172 (2016) 248–252. doi:10.1016/j.fuel.2016.01.030.

[40] P. C. Malte, D. T. Pratt, The role of energy-releasing kinetics in NO_x formation: fuel-lean, jet-stirred CO-Air combustion, Combust. Sci. Technol. 9 (5-6) (1974) 221–231. doi:10.1080/00102207408960360.

[41] M. Ihme, H. Pitsch, Modeling of radiation and nitric oxide formation in turbulent nonpremixed flames using a flamelet/progress variable formulation, Phys. Fluids 20 (5) (2008) 055110. doi:10.1063/1.2911047.

[42] J. Schwenk, A. Khandelwal, M. Fratkin, V. Kumar, E. Foufoula-Georgiou, High spatiotemporal resolution of river planform dynamics from Landsat: The RivMAP toolbox and results from the Ucayali river, Earth Space Sci. 4 (2) (2017) 46–75. doi:10.1002/2016EA000196.